UNIVERSITY OF TWENTE.

Faculty of Engineering Technology - Department of Thermal and Fluid Engineering

Master Thesis

Applying a RANS-based Multiphase and Phase Change CFD Model to Simulate a Venturi-Driven Milk Foamer

Author:
Jasper Wijnen

Graduation Committee:
prof.dr.ir. W. Rohlfs
dr. P. Ströer
dr. T. Zhu
ir. I. Cleine-Koopmans

December 2024

Acknowledgements

I would like to express my gratitude to my committee for all their support during my research. I would particularly like to thank my supervisors, both at the University of Twente and at Demcon Multiphysics, where this research was carried out, for their valuable help, patience, and feedback. Lastly, I would like to extend my sincerest gratitude to Versuni for their generous support and guidance throughout this graduation project. Their willingness to offer the topic as a graduation project allowed me to research an everyday device with complex multiphysical workings, something that was of great interest to me. Additionally, I appreciate the valuable assistance provided by their team members along the way, which greatly contributed to the success of my research.

Abstract

In coffee machines, a venturi injector can be used to produce milk foam for various kinds of coffee. In this thesis, the process of creating suction and heating milk will be investigated using experimental and numerical methods. The goal of this research is to gain insight into the physics of the milk foaming process in a Venturi-driven milk foamer, with a specific focus on heat transfer between the two phases, the resulting phase change, and its impact on the pressure and flow fields.

This is achieved by developing a numerical model using a RANS-based Eulerian multiphase solver with an additional Boiling/Condensation solver in the simulation software Siemens Star CCM+. A multiphase model was built up and validated according to the thermodynamic expectation from steam tables. The accuracy of the model was found to depend on the rate of heat and mass exchange, which could be altered by varying the interactive length scale (mean bubble size). This parameter is calibrated using data obtained from an experiment. An additional experiment is conducted, which used pressure, suction mass flow rate, and temperature measurements to validate both the flow and thermal behaviour of the numerical Venturi-driven milk foamer.

The numerical model underestimates the ratio of suction mass flow to outlet mass flow by 30% compared to the experiment. Despite this, the numerical model gives good physical insight into the flow field, how condensation takes place in and after the neck, and how this impacts the results.

Contents

1 Introduction

In 2022, 79% of Dutch inhabitants aged 16 or older drank coffee regularly, with 63% consuming it on a daily basis [1]. Next to black coffee, the dutch like to drink their coffee as a cappuccino, which consists of 1/3 coffee, 1/3 milk and 1/3 milk foam [2]. There are different ways of producing the milk foam, one of them being the venturi suction method.
Modern electric coffee machines such as the Philips LatteGo use a venturi driven system to generate the milk foam used in its various coffee drinks. Such a system uses saturated steam (part water, part steam) to create an underpressure that draws milk from a reservoir into the steam flow. Steam is also used to heat up the milk. In addition to milk, air is also injected into the mixture and creates the milk foam. Research up to now has focused on the use of venturi injectors for agricultural applications including both experimental and numerical models. However, these are operated in a drastically different environment to an injector for milk foaming capabilities. Their geometry is larger, they are one-phase without heat transfer and they operate with lower velocities.
To design more effective venturi-driven milk foamers, the complex physics of heat transfer between the two phases, the resulting phase change, and its impact on the pressure and flow fields must be understood.
The goal of this research is to investigate the possibility to numerically model a venturi injector at the conditions required for a milk foamer and gain insights into the relevant physical phenomena. This paper focuses specifically on the act of injecting milk into the mixture, excluding air injection and foam modelling.
A numerical simulation requires multi-phase modelling to investigate the suction of milk by a saturated steam and subsequent heat transfer between them. Furthermore, phase change caused by fluid interaction needs to be modelled. The commercial software Siemens Star CCM+ will be used for this purpose.

This research is divided into four main sections.
In section 2, the background of milk foaming, and better understanding of how a venturi driven milk foamer is used to efficiently foam milk is investigated. Furthermore, this section discussed the relevant theory to describe the pressure differences that occur within the venturi channel and the background of the numerical model. In section 3, the methodology of both the planned experiments and numerical set up for the research is discussed.
Within the results of section 5, the separate parts of physics which occur within the venturi milk frother are modelled and validated according to analytical/empirical calculations and existing experimental data from literature. This creates the opportunity to understand where any differences originate from, and the effect of certain assumptions and parameters on the results of the Computational Fluid Dynamics (CFD) model, which are discussed in subsection 5.4. There the physics is brought together to build a numerical simulation which models a venturi injector for milk foaming applications. The results of subsection 5.4 are tuned and compared to the experimental results in section 4.

2 Background

This section reviews existing research relevant to our study, encompassing three key areas: the formation of milk foam, physical flow effects, and modelling approaches.

2.1 Creating a Milk Foam

Foam formation occurs when air is trapped within a liquid, such as milk, resulting in a dispersed gas surrounded by a continuous liquid. The amount of foam that forms depends on the quantity of air introduced into the liquid and the liquid's inherent foaming properties. Milk foams can be created through various methods:

- **Injection** - This method involves injecting gas or steam into the milk using a nozzle. Using steam has the added benefit of heating up the milk [3].
- **Agitation** - In this approach, foam is formed by agitating the milk and transferring mechanical energy. A common example is a specialised whisking device designed specifically for milk foaming [3].
- **Supersaturation** - Lastly, this method involves applying pressure to the milk to dissolve a gas within it. When the pressure is released, foam forms [4]. According to Walstra's book, this method is not typically applied in food emulsions.

The two primary methods for foaming milk in coffee applications are mechanical agitation or steam injection. While mechanical agitation produces a more stable foam, steam injection generates a stronger milk foam that is less sensitive to the type of milk used [5]. Additionally, steam injection can be integrated into the coffee machine itself, whereas mechanical agitation often requires an additional device from the machine. The venturi milk frother discussed in this thesis falls under the category of steam injection methods and is part of a coffee machine design that enables users to create a coffee such as cappuccinos without requiring an additional process to generate the foam. Figure 2.1 illustrates such a coffee machine.

Figure 2.1: Philips LatteGo with Integrated Milk Foamer [6].

The actual design of such a venturi injector can be visualised in Figure 2.2. This is a small part, the neck diameter is only 1.2 mm. This device employs saturated steam (a mixture of water and steam) to create an under-pressure within the neck, drawing milk from a reservoir into the steam flow. The steam also serves to heat up the milk. Additionally, air is injected into the mixture, generating the milk foam.
The operation of this venturi injector can be broken down into three main components, as labelled in Figure 2.2: (1) the use of saturated steam as a working fluid, discussed further in subsection 2.2; (2) the venturi effect, explored in subsection 2.3; and (3) the creation of milk foam, examined in subsection 2.4.

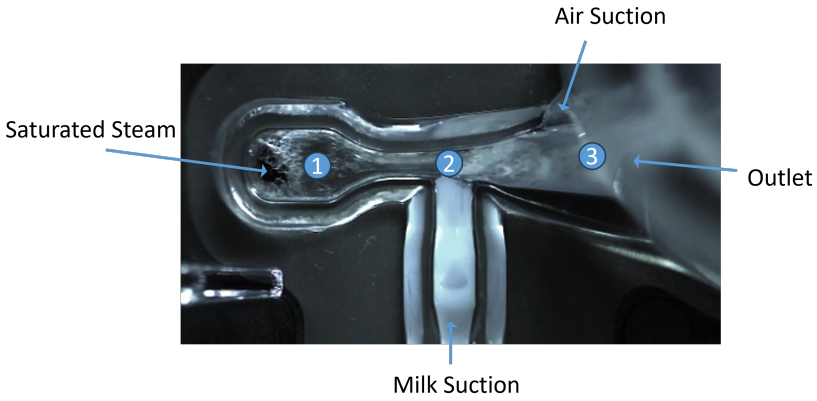

Figure 2.2: Steps of a Venturi Driven Milk Foamer.

2.2 Saturated Steam

Saturated steam is employed in venturi-driven milk foamers due to its ability to achieve high velocities within the neck, thereby generating large underpressures. Additionally, saturated steam contains the necessary energy to heat the suctioned milk. However, it is not feasible to model saturated steam as a single phase using Star CCM+. Instead, a multiphase approach is required to simulate this fluid behavior. Furthermore, since the ratio of the two phases (water and vapour) varies throughout the domain, a boiling-condensation model must be employed to model the transfer of heat and mass between these phases.

2.2.1 Thermodynamics of Saturated Steam

The venturi milk frother distinguishes itself from other venturi injectors, due to the thermodynamic effects that occur within it. The working fluid is saturated steam, which consists of two phases mixed together - water and vapour. Furthermore, there is a large temperature difference between the saturated steam and the suction fluid, leading to heat transfer between the fluids and condensation of the steam. The properties of the bulk steam also change throughout the geometry, for example, in the neck of the venturi tunnel where static pressure reduces. The properties of water, the vapour dome, and thermodynamic tables can be found in "Thermodynamics: An Engineering Approach" [7] or using codes such as XSteam [8]. From these resources the behaviour of the fluid during pressure changes can be predicted. In the case of constant enthalpy, a pressure drop in the neck results in a drop in temperature and an increase in steam quality, meaning more fluid has transitioned to the vapour state. This can be visualised with the pressure-enthalpy diagram in Figure 2.3.

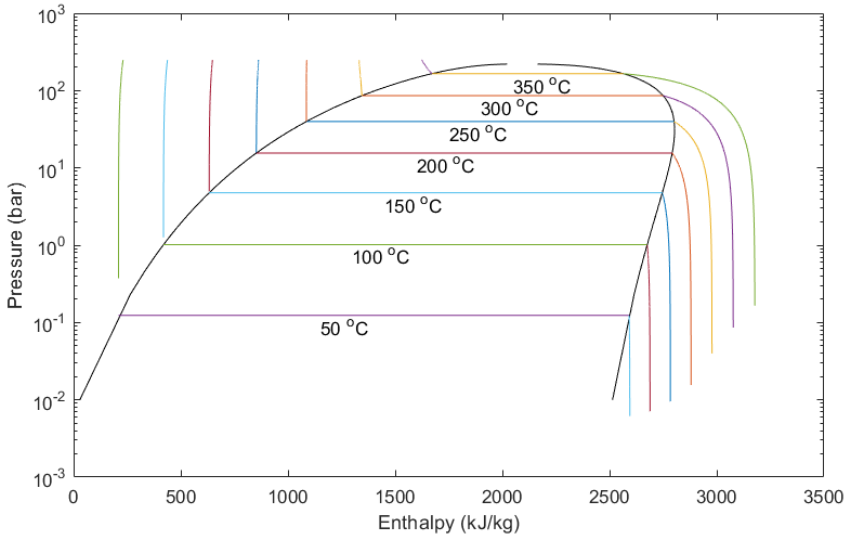

Figure 2.3: Pressure Enthalpy Curve Water.

2.2.2 Multi-Phase Modelling

The selection of a multi-phase model depends on the specific application and requirements. These models can be categorised into two groups: those using the Eulerian method and those employing the Lagrangian method [9]. The Lagrangian method tracks individual particles [10], making it more computationally intensive [11], whereas the Eulerian method applies conservation equations to each fluid volume phase [10]. In the context of the venturi injector application, tracking individual particles is not necessary. Instead, modelling the distribution between gas and liquid phases, and their fluid properties like temperature, is sufficient. The Eulerian method is therefore a more suitable choice. Within the Eulerian multi-phase method there are several options available within Star-CCM+, namely [9]:

- The Mixture Multiphase Model (MMP)
- The Volume of Fluid Model (VOF)
- The Eulerian Multiphase Model (EMP)

The MMP model is a simplified model of the Eulerian Multiphase Model that treats mass, momentum, and energy as mixture quantities rather than phase quantities [9]. The transport equations are solved for the mixture as a whole. The MMP model is intended to be used when the grid the solution is being solved on is coarser than the interface between phases. Therefore, even on a fine grid, a sharp interface between phases is not resolved.
The Volume of Fluid Model (VOF) models immiscible fluids with each phase having a large structure and a relatively small contact area [9]. Examples of its application include sloshing water or oil and water mixtures. As the fluids of water and steam are not immiscible and have a strong influence on each other during the phase change, the VOF model is not suitable for the case of the venturi milk frother.
The EMP model is the most complete Eulerian multiphase solver. Each phase has its own set of conservation equations (mass, momentum, and energy) discussed in subsubsection 2.5.1. Both phases share a pressure field. Importantly, the EMP model has the ability to model boiling and condensation. This allows for a transfer of mass, momentum and energy between the two phases [9].

2.2.3 Boiling-Condensation Modelling

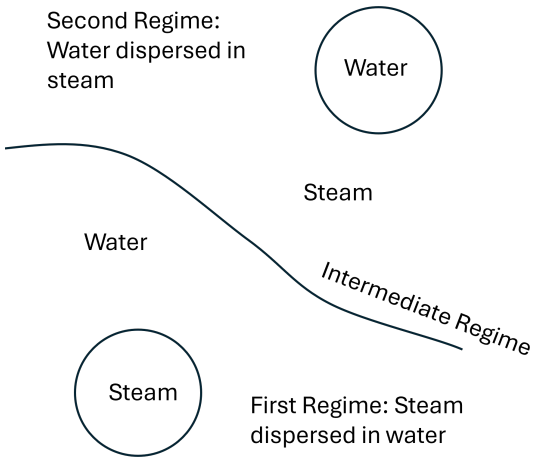

(a) Regimes of Two-Phase Flow.

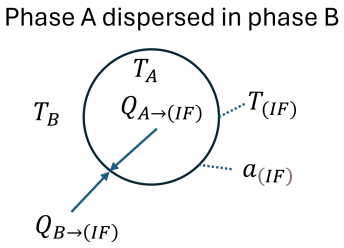

(b) Heat Transfer From Phases to the Interface.

Figure 2.4: Two-Phase Flow Regimes and Heat Transfer Between Two Phases [9].

To model the phase change between water and steam, a phase change model must be used. The boiling/condensation model in Star CCM+ allows for the transfer of mass, momentum, and energy between the two phases [9]. The Boiling-Condensation model requires specific properties to define the rate of phase change and the boiling temperature [9]. The boiling temperature is defined using the IAPWS-IF97 water model. The IAPWS-IF97 model is also used for the steam tables discussed in subsubsection 2.2.1. The IAPWS-IF97 model enables characteristics such as the boiling point to vary as a result of the pressure of the system.

The rate of phase change is defined by the heat transfer between phases. The heat transfer between phases is defined for three regimes; two dispersed regimes and an intermediate regime. These are visualised in Figure 2.4a. The general formulation for heat transfer from phase (A) to the interface (IF) is:

$$Q_{A\to(IF)} = h_{A\to(IF)} \cdot a_{(IF)} \cdot \left(T_{(IF)} - T_A\right). \tag{2.1}$$

Similarly, the heat transfer from the phase (B) to the interface (IF) is:

$$Q_{B\to(IF)} = h_{B\to(IF)} \cdot a_{(IF)} \cdot \left(T_{(IF)} - T_B\right) \tag{2.2}$$

as defined by the Star CCM+ documentation[9]. The heat transfer between phases is also shown visually in Figure 2.4b. Where T_A and T_B are the temperatures of the continuous and dispersed phase, and $T_{(IF)}$ the temperature of the interface between the two phases, this is often defined as the saturation temperature. The area over which the heat transfer takes place is denoted by the coefficient $a_{(IF)}$. The heat transfer coefficient (h) must be defined:

$$h_{A\to(IF)} = \frac{\mathrm{Nu}_A \cdot k_A}{l_{(IF)}} \tag{2.3}$$

$$h_{B\to(IF)} = \frac{\mathrm{Nu}_B \cdot k_B}{l_{(IF)}} \tag{2.4}$$

where Nu is a Nusselt Number, k the thermal conductivity and l the interactive length scale. The Nusselt Number is determined empirically, and various models are possible for calculating this value. For the case of the continuous phase in the two dispersed regimes the Ranz-Marshall correlation [12] is used:

$$\mathrm{Nu} = 2 + 0.6\mathrm{Re}_d^{0.5}\mathrm{Pr}_c^{0.3} \tag{2.5}$$

as advised by Star CCM+ documentation[9]. Where Re_d is the Reynolds number of the dispersed phase,

$$\mathrm{Re}_d = \frac{\rho_d l_d \left(|u_c - u_d|\right)}{\mu_d} \tag{2.6}$$

and Pr_c the Prantl number of the continuous phase,

$$\mathrm{Pr}_c = \frac{\nu_c}{\alpha_c} \tag{2.7}$$

where, ν and α and the kinematic viscosity and the thermal diffusivity respectively.
Unfortunately, this Nusselt Number definition cannot be used for the dispersed side of the interface. From Ansys documentation [13], an alteration to the Ranz-Marshall is used for the dispersed side. This replaces the $0.3\mathrm{Pr}^{0.3}$ term with the constant 0.23,

$$\mathrm{Nu} = 2\left(1 + 0.23\mathrm{Re}_d^{0.5}\right). \tag{2.8}$$

For the intermediate regime, the Hughes and Duffey Correlation is used [9, 14]. The Nusselt number is defined as:

$$\mathrm{Nu} = \frac{2}{\sqrt{\pi}}\mathrm{Re}_t\mathrm{Pr}^{0.5} \tag{2.9}$$

where Re_t is the turbulent Reynolds number,

$$\mathrm{Re}_t = \frac{\rho l_t u_t}{\mu} \tag{2.10}$$

determined by turbulent length (l_t) and velocity scales (u_t) from the turbulence model. However, this approach may only be used to define the Nusselt number on the liquid side of the interface. It is not possible to find an approximation for the gas side of the interface; therefore, a sensitivity analysis is conducted on this Nusselt number to determine its potential impact on the results.

The heat flux can then be calculated using Equation (2.1) and Equation (2.2). In the case of Star CCM+ this is done by defining the Nusselt Numbers as field functions, calculating them for each cell. Depending on the volume fraction, the correct Nusselt Number is assigned to the equation.
The mass flow rate between the two phases is defined by the heat flux between the two phases as[9]:

$$\dot{m} = -\frac{Q_{A\to(IF)} + Q_{B\to(IF)}}{\Delta h_{AB}}. \tag{2.11}$$

Where Δh_{AB} is the enthalpy difference between the two phases.
The heat and mass flow rates can then be added as source terms in the conservation equations discussed in subsubsection 2.5.1.

2.3 Venturi Flow

The venturi milk frother uses partial steam as the working fluid, which flows through a venturi tunnel. The decrease in static pressure within the neck creates a suction pressure and therefore mass flow from the suction inlet, injecting the milk into the steam. The method by which milk is injected is comparable to the method used to mix fertilisers with water for agricultural use as seen in Figure 2.5. In the case of a venturi milk foamer, the working fluid, steam, enters through the inlet on the left, while milk enters via the suction inlet due to an underpressure within the throat.

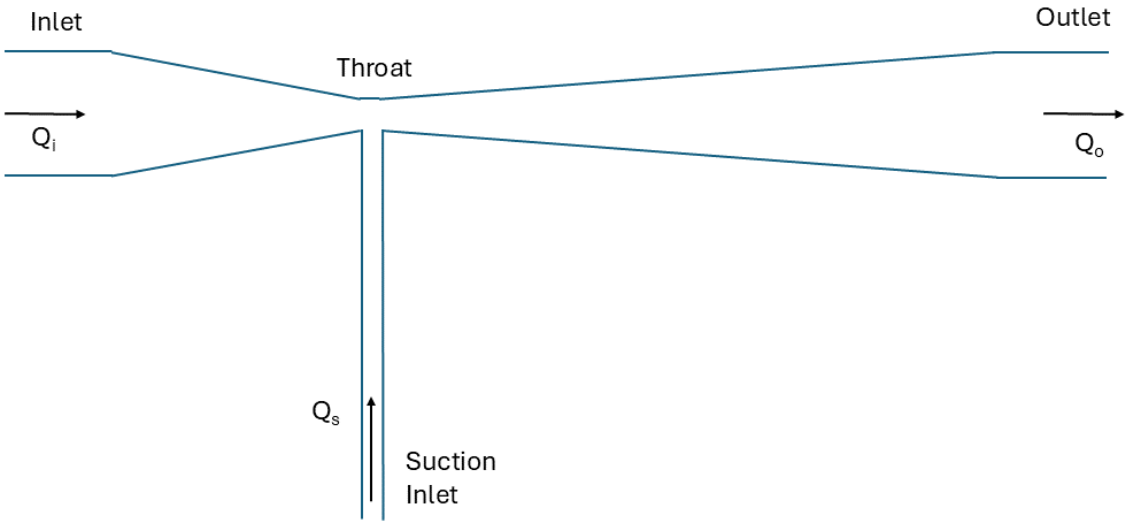

Figure 2.5: Geometry of a Venturi Injector.

This method is widely used in fertiliser irrigation due to its cheap and robust system which does not have moving parts to service [15]. For this application, extensive research has been done analytically, experimentally, and with CFD.

2.3.1 Pressure Drops

The effect of reducing the static pressure in the neck of the venturi tunnel is described by Bernoulli [16, 17]. The Bernoulli principle states that the material derivative of the simplified momentum equation is 0,

$$\frac{D}{Dt}\left[\frac{p}{\rho}+\frac{1}{2}u_j u_j + g\zeta\right] = 0. \tag{2.12}$$

As the venturi tunnel is aligned solely in the x direction, it is unaffected by the gravitational component. Therefore, this is simplified further to, total pressure is constant along streamlines:

$$p+\frac{1}{2}\rho u^2 = C.A.S. \tag{2.13}$$

Therefore, if the velocity increases, the dynamic pressure,

$$p_d = \frac{1}{2}\rho u^2 \tag{2.14}$$

will increase. As the total pressure according to Bernoulli must remain constant, the static pressure, p, must decrease. The Bernoulli expression is commonly employed in research on venturi injectors. However, it should be noted what the assumptions are. Using the Bernoulli simplified momentum equation, it is assumed that the fluid is **Steady, Incompressible, and Inviscid**. Although neglecting viscosity can simplify the problem, it may not always be reasonable. The venturi tunnel used in a device such as the LatteGo is only a few mm in diameter at the neck. This may mean neglecting the viscosity has a larger effect than is reasonable.

Beyond the increase in dynamic pressure leading to a drop in static pressure, there are additional factors that contribute to a decrease in static pressure. These are referred to as total pressure resistances. For instance, the frictional losses neglected in the Bernoulli equation. These additional resistances are resistances to the total pressure; therefore, there will always be

a drop in total pressure along the domain due to these resistances. The pressure resistance due to friction is calculated using the Darcy-Weisbach equation as follows:

$$\Delta p_f = \lambda \frac{L}{D_h} \frac{\rho u^2}{2} = \zeta_f \frac{\rho u^2}{2}. \tag{2.15}$$

This allows for an estimation of pressure losses along a straight tube [18]. The friction coefficient is a function of the Reynolds number. Where the coefficient λ is determined empirically. λ varies according to Reynolds number.

$$\lambda = \frac{64}{Re} \qquad \text{For Re} < 4000 \tag{2.16}$$

$$\lambda = \frac{0.3164}{Re^{0.25}} \qquad \text{For } 4000 < \text{Re} < 1\text{e}5 \tag{2.17}$$

$$\lambda = \frac{1}{\left(1.8 \ln\left(Re\right) - 1.64\right)^2} \qquad \text{For Re} > 1\text{e}5 \tag{2.18}$$

Similarly, additional pressure resistance terms can be calculated to predict pressure drops that occur in a converging nozzle [18, 19]. The first additional resistance term is the contraction resistance [18], which occurs due to the necking of the venturi tunnel. This term depends on the geometry of the tunnel, specifically the change in area before and after the contraction, as well as the shape of the transition between these two regions. These are seen in Figure 2.6. Both the rounded and bevelled transitions are used for venturi tunnels. In the case of a rounded transition, the pressure resistance coefficient is defined as:

$$\zeta_c = \zeta' \left(1 - \frac{A_0}{A_1}\right)^{\frac{3}{4}} \tag{2.19}$$

where,

$$\zeta' = 0.03 + 0.47 \times 10^{-7.7\bar{r}} \tag{2.20}$$

and,

$$\bar{r} = \frac{r}{D_h}. \tag{2.21}$$

For a bevelled transition, the pressure resistance ζ_c is defined as:

$$\zeta_c = \left(-0.0125 n_0^4 + 0.0224 n_0^3 - 0.00723 n_0^2 + 0.00444 n_0 - 0.00745\right)\left(\alpha_r^3 - 2\pi\alpha_r^2 - 10\alpha_r\right) \tag{2.22}$$

where,

$$n_0 = \frac{A0}{A1} \tag{2.23}$$

and,

$$\alpha_r = 0.0349\alpha. \tag{2.24}$$

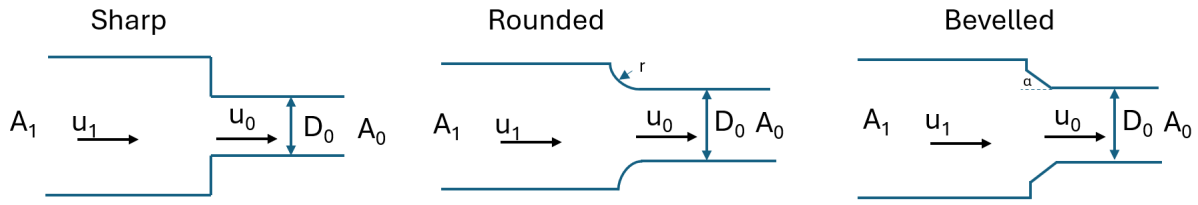

Figure 2.6: Types of Neck Transitions [18].

A second term of pressure resistance arises from the addition of a second fluid joining the main flow stream. In the case where a main straight passage is joined by a second secondary flow

without an increase in cross-sectional area, as illustrated in Figure 2.7, the resistance is defined as:

$$\zeta_j = 1 - \left(1 - \frac{Q_s}{Q_0}\right)^2 - \left(1.4 - \frac{Q_s}{Q_0}\right)\left(\frac{Q_s}{Q_0}\right)^2 \sin\alpha - 2K'_{st}\frac{A_0}{A_s}\frac{Q_s}{Q_0}\cos\alpha \tag{2.25}$$

by Idelchik[18]. Where Q_s is the volume flow rate of the joining flow, Q_C the volume flow rate of the combined stream, K'_{st} is a coefficient found in a table within the handbook of Idelchik [18]. α is the angle of the joining flow.

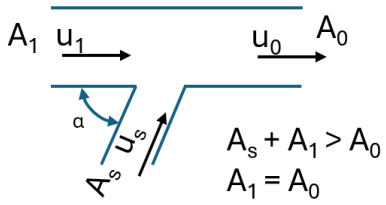

Figure 2.7: Additional Fluid Stream Entering the Main Stream [18].

The resistance coefficients are then used to calculate the total pressure resistance,

$$\Delta p_r = \zeta \frac{\rho u^2}{2}. \tag{2.26}$$

This result appends Equation (2.13) to:

$$p_{t,1} = p_{t,2} + \Delta p_r. \tag{2.27}$$

Furthermore, there is an expectation that the condensation of the working fluid in the diffuser impacts the pressure in the neck. The working fluid used is saturated steam, this means that the flow contains two phases, water and steam. For an analytical approach, it must be assumed that the flow is homogeneously well mixed [16]. This means that the gas and water have the same velocity, and properties of the mixture, such as density, are determined by taking the volume average. These quantities are used to calculate the static pressure drop and contraction resistance. This same assumption allows a two-phase correction multiplier to be applied for the friction resistance. The correction factor is made following the Lockhart-Martinelli model [20] and simplified by D. Chisholm [21]. This model is proposed for a combination of gas and liquid flow in pipes [22]. The friction multiplier ϕ_G is defined as:

$$\phi_G^2 = \mathbf{X} \cdot \phi_L^2 \tag{2.28}$$

where,

$$\phi_L^2 = 1 + \frac{C}{\mathbf{X}} + \frac{1}{\mathbf{X}^2}. \tag{2.29}$$

and $\mathbf{X}$ is the non-dimensional Lockhart-Martinelli parameter, defined as:

$$\mathbf{X}^2 = \frac{\Delta p_L}{\Delta p_G}. \tag{2.30}$$

Where Δp_L and Δp_G are the frictional pressure drops due to the liquid and vapour flows independently. The coefficient C is determined experimentally for various cases, however a standard set of values is seen in Table 2.1 [23].

Table 2.1: Friction Multiplier Constant C.

Liquid	Gas	C
Turbulent	Turbulent	20
Viscous	Turbulent	12
Turbulent	Viscous	10
Viscous	Viscous	5

The pressure resistance of the two-phase mixture is then described as:

$$\Delta p_{\text{mix}} = \Delta p_G \phi_G^2. \tag{2.31}$$

2.3.2 Suction of Fluid

The underpressure created by the venturi effect draws milk from a reservoir. The mass flow rate is defined by the pressure difference between the suction inlet and the neck, taking into account the frictional pressure resistance along the suction tube. As the milk mixes with the steam, heat transfer occurs between the two phases. To determine the final temperature of the mixture, the power input of the two incoming streams is set equal to the power of the outgoing stream. From there the mixture enthalpy can be calculated. Lastly, using the known pressure, the temperature of the mixture is calculated using steam tables. This conservation equation for two joining streams is expressed as:

$$\begin{aligned} \dot{E}_1 + \dot{E}_2 &= \dot{E}_{1+2} \\ \dot{m}_1 h_1 + \dot{m}_2 h_2 &= (\dot{m}_1 + \dot{m}_2)\, h_{1+2} \end{aligned} \tag{2.32}$$

where, $\dot{m}$ and h are the mass flow and enthalpy respectively, as stated by Cengel [7].
The time it takes for the fluid to reach final thermal equilibrium, or even the point of full condensation, is challenging to predict, as it is determined by how the milk and steam mix. The impact of condensation on the pressure is also harder to predict due to the variability of how and where it forms.

2.4 Milk Foam

To understand the workings of the venturi injector, its objectives when generating milk foam must first be understood. Foaming properties of milk foam are well documented in the review of Huppertz [3] and is the basis for much of the research in subsection 2.4.

2.4.1 Generating Foam

Despite being 88% water [24], milk is more foamable than water. This is due to the presence of surfactants. These lower the surface tension between gas and water, which allows the formation of gas bubbles to occur more easily [3]. In milk these surfactants are casein proteins (80%) and whey proteins (20%) [24]. To quantify the quality of foam, it is important to have consistent measurement criteria. Common parameters used to determine the quality of milk are [3]:

- **Foamability** - The amount of foam created from a volume of milk. Denoted as a percentage, volume of foam/starting milk volume.
- **Foam Stability** - The ability to retain its volume over time, defined by the half-life.
- **Bubble Size** - The average size and size distribution of the foam bubbles.

- **Overrun** - The amount of air that is entrapped within the foam. Closely linked to the density of the foam. As the overrun increases, the density of the foam will decrease. As with bubble size, a lower level of overrun will lead to more stable, dense foam [25].

2.4.2 Influence of Temperature

The temperature of the milk has a strong influence on the foam quality. The foamability of skim-milk increases with increasing temperature, as seen in Figure 2.8a [26]. The studies theorise that this is due to the decreasing surface tension with increasing milk temperature. On the other hand, foam overrun and average bubble diameter decrease with increased temperature [27, 28]. Stability is shown to have a clear optimum around 45 °C as seen in Figure 2.8b [26]. Therefore, it is desired to heat milk to improve the quality and quantity of foam.

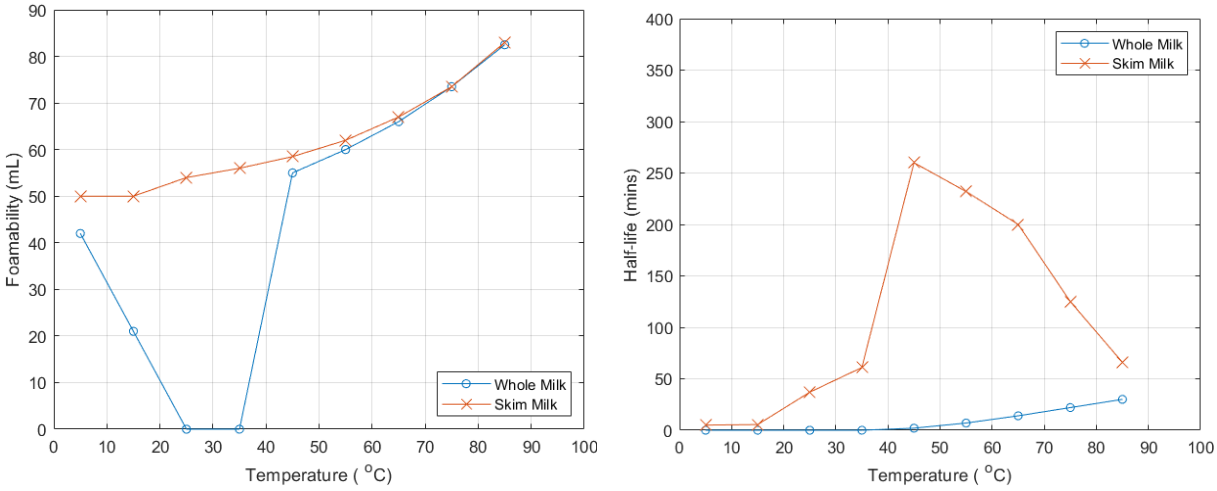

(a) Foamability

(b) Half Life

Figure 2.8: Foam Qualities as a Function of Temperature [26].

2.4.3 Influence of Fat

Figure 2.8 also illustrates the influence of fat within the milk. Even small amounts of fat in the mixture destabilise the formation and stability of foam in the sub 40 °C temperature range [26, 28]. This makes it challenging to create stable foam that lasts for even a few minutes [26]. This is likely due to the crystalline state of the fat below 40 °C [3]. The partially crystalline state of milk is more susceptible to shear-induced disruptions, leading to liquid fat spreading over the air bubbles, which lead to bubble coalescence. At temperatures above 40 °C, there is a near absence of crystalline structure. This reduces the chance of fat globule rupture [3].
At temperatures higher than 50 °C at the time of foaming there is a smaller difference measured between skimmed and whole milk [26, 28].
Common heat treatments improve the weak foam quality of fatty milk at low temperatures. Ultra high temperature (UHT) treatment, which involves heating milk up to 138 °C-150 °C for one or two seconds [29], being the most effective. Standard pasteurisation also shows improvements, mostly in stability over raw whole milk. This process also involves heating the milk to an elevated temperature, to kill bacteria and improve shelf life. However, this is at a temperature of 63 °C for 30 minutes or 72 °C for 15 seconds [29].

2.4.4 Modelling Milk

To model a venturi milk frother, the material properties of milk must be known. Milk is 88% water [7], therefore, the simplest approach is to assume that it behaves like water. However,

this is not the case for all properties. This is seen in the results of experimental work [30]. The properties of skim and whole milk compared to water for varying temperature are shown in Figure 2.9.

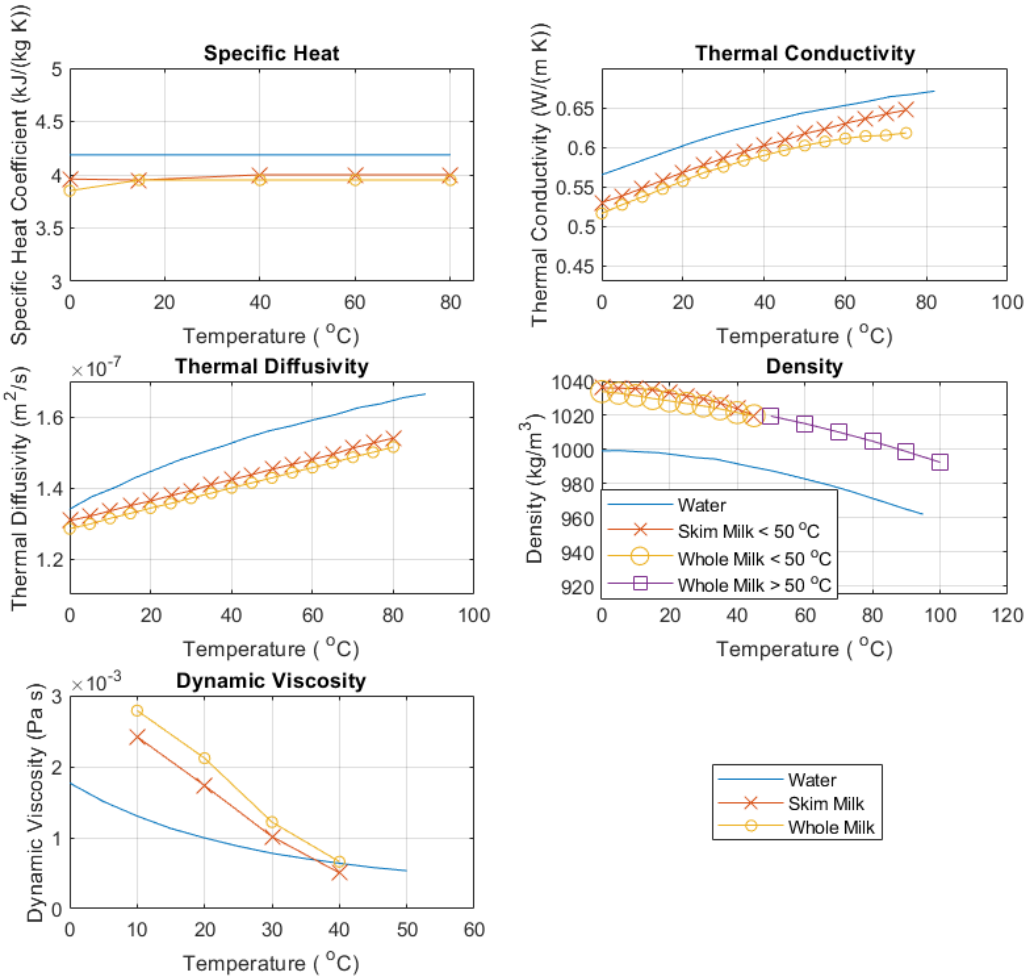

Figure 2.9: Properties of Milk Compared to Water

Thermodynamic data such as the saturation pressure and temperature at all pressures and temperatures is unfortunately not available for milk. Furthermore, despite the differences, the fundamental process required for the goal of this research can be understood with water. Therefore, it is chosen to model and experiment the system using water as a suction fluid.

2.5 Numerical Modelling

2.5.1 Fundamental Equations

The fundamental equations that form the basis of CFD code are the conservation of:
mass,

$$\frac{\partial \rho}{\partial t} + \frac{\partial \left(\rho u_j\right)}{\partial x_j} = 0, \tag{2.33}$$

momentum,

$$\frac{\partial \left(\rho u_i\right)}{\partial t} + \frac{\partial}{\partial x_j}\left(\rho u_i u_j\right) = -\frac{\partial}{\partial x_j}\left(p\delta_{ij}\right) + \frac{\partial \tau_{ij}}{\partial x_j} + \rho g_i, \tag{2.34}$$

and energy,

$$\frac{\partial(\rho E)}{\partial t}+\frac{\partial}{\partial x_j}(\rho E u_j)=-\frac{\partial}{\partial x_j}(p u_j)+\frac{\partial}{\partial x_j}(\tau_{ij}u_i)-\frac{\partial q_j}{\partial x_j}+\rho g_j u_j+S_E. \tag{2.35}$$

Where ρ is the density, t is time, u is velocity, p is pressure, δ is a kronecker delta, τ is a stress tensor, g is a gravitational constant, E is the total specific energy, q is the heat flux and S_E describes any energy source terms as defined by Star CCM+ documentation and derived by Anderson [9, 31].

2.5.2 Reynolds Averaged Simplification and Multiphase Adaptation

The conservation equations 2.33 to 2.35 are time averaged to simplify the computational requirement. This is done by splitting a quantity (γ) into an averaged component ($\overline{\gamma}$) and a fluctuating component (γ').

$$\gamma=\overline{\gamma}+\gamma' \tag{2.36}$$

Furthermore, additional terms for the transfer of mass and energy between phases (a) and (b) are included. The conservation equations are solved for each fluid phase independently, those for phase (a) are adapted according to the Star CCM + documentation [9], to the following:
mass,

$$\frac{\partial \alpha\rho}{\partial t}+\frac{\partial(\alpha\rho\overline{u_j})}{\partial x_j}=m_{b\to a}-m_{a\to b}, \tag{2.37}$$

momentum,

$$\frac{\partial(\alpha\rho\overline{u_i})}{\partial t}+\frac{\partial}{\partial x_j}(\alpha\rho\overline{u_i u_j})=-\frac{\partial}{\partial x_j}(\alpha\overline{p}\delta_{ij})+\frac{\partial}{\partial x_j}\alpha\left(\overline{\tau_{ij}}+\tau_{ij}^{\mathrm{RANS}}\right)+\alpha\rho g_i + (M_i+m_{b\to a}\overline{u_{b,i}}-m_{a\to b}\overline{u_{a,i}}) \tag{2.38}$$

and energy,

$$\frac{\partial\left(\alpha\rho\overline{E}\right)}{\partial t}+\frac{\partial}{\partial x_j}\left(\alpha\rho\overline{E}\overline{u_j}\right)=-\frac{\partial}{\partial x_j}(\alpha\overline{p u_j})+\frac{\partial}{\partial x_j}\left(\alpha\left(\overline{\tau_{ij}}+\tau_{ij}^{\mathrm{RANS}}\right)\overline{u_i}\right)-\frac{\partial\alpha\overline{q_j}}{\partial x_j} + f_j\overline{u_j}+Q_{b\to a}+Q_{a\to(IF)}+(m_{b\to a}-m_{a\to b})\,h_a+S_E. \tag{2.39}$$

Where α is the volume fraction, $m_{b\to a}$ the mass transfer rate per unit volume from phase b to phase a, M the interface momentum transfer per unit volume (the sum of forces the phases exert on each other), f the body force per unit volume (which includes all external forces such as gravity and interphase forces), $Q_{b\to a}$ the heat transfer rate per unit volume from phase a to phase b due to a temperature difference, $Q_{a\to(IF)}$ the heat transfer rate per unit volume from phase a to the phase interface due to heat transfer phenomena such as boiling and condensation, and h_a the enthalpy of phase a at the saturation temperature.
The conservation of energy equations of the two phases are linked with a third equation which defines the addition of latent heat:

$$Q_{a\to(IF)}+Q_{b\to(IF)}+(m_{b\to a}-m_{a\to b})\,\Delta h=0. \tag{2.40}$$

Where Δh is the enthalpy difference between the two phases.
The turbulent stress tensor, $\tau_{ij}^{\mathrm{RANS}}$, is defined using a turbulence model [32]. The simplest choice and one of many research papers for agricultural venturi injectors is an eddy viscosity model such as the k-ϵ model. This model solves the transport equations as defined by Star CCM+ documentation [9], for the turbulent kinetic energy (k):

$$\frac{D(\rho k)}{Dt}=\frac{\partial}{\partial x_j}\left[\left(\mu+\frac{\mu_t}{\sigma_k}\right)\frac{\partial k}{\partial x_j}\right]+P_k-\rho(\epsilon-\epsilon_0) \tag{2.41}$$

and the dissipation rate (ϵ):

$$\frac{D(\rho\epsilon)}{Dt} = \frac{\partial}{\partial x_j}\left[\left(\mu + \frac{\mu_t}{\sigma_\epsilon}\right)\frac{\partial \epsilon}{\partial x_j}\right] + \frac{1}{T_\epsilon}C_{\epsilon 1}P_\epsilon - C_{\epsilon 2}\rho\left(\frac{\epsilon}{T_\epsilon} - \frac{\epsilon_0}{T_0}\right). \tag{2.42}$$

Where μ is the dynamic viscosity, μ_t the turbulent viscosity, P_k and P_ϵ are production terms, T_e is the large eddy time scale $\left(\frac{k}{\epsilon}\right)$, ϵ_0 and T_0 are ambient dissipation and time scale values, and σ_k, σ_ϵ, $C_{\epsilon 1}$, $C_{\epsilon 2}$ are model coefficients. The turbulent kinetic energy and dissipation rate are used to calculate a turbulent eddy viscosity μ_t:

$$\mu_t = \rho C_\mu k T. \tag{2.43}$$

Where C_μ is a model coefficient and;

$$T = \max\left(T_\epsilon, C_t\sqrt{\frac{\nu}{\epsilon}}\right). \tag{2.44}$$

Where ν is the kinematic viscosity and C_t is a model coefficient. The turbulent stress tensor is then modelled according to the Boussinesq assumption:

$$\boldsymbol{\tau}^{\mathrm{RANS}} = 2\mu_t\mathbf{S} - \frac{2}{3}\left(\mu_t\nabla\cdot\overline{\mathbf{v}}\right)\mathbf{I} \tag{2.45}$$

Where $\mathbf{S}$ is the mean strain rate tensor:

$$\mathbf{S} = \frac{1}{2}\left(\nabla\overline{\mathbf{v}} + \nabla\overline{\mathbf{v}}^T\right) \tag{2.46}$$

and $\mathbf{I}$ the identity matrix.

2.6 Current State of Research

The concept of converging/diverging channels has been studied since Bernoulli's investigation in 1738 [17]. In 1887 Herschel demonstrated the use of a venturi tube to measure liquid flow rates by applying the Bernoulli principal. The coupling between the static pressure and the velocity allows a flow rate to be calculated [33].

The application of venturi channels extends beyond measuring flow rates. The change in static pressure in the neck allows for drawing of a second fluid. A major use of this application and a focus of research is for the agricultural industry to draw fertiliser into a water stream during irrigation. Additionally, this technology is employed in multiphase applications, injecting gases like air into pressurised water systems [34]. The effectiveness of these applications has been investigated both experimentally [34] and numerically [35]. With CFD able to reproduce experimental results within 5% [15, 35]. The use of numerical simulations enables rapid investigation into various geometrical properties to optimise the mixing process, which is more efficient than experimental studies. In the study of Zhang, the amount of suction mass flow could be tripled by replacing a singular suction tube with two suction ports at an angle of 24^o from the horizontal. Parametric studies using numerical tools revealed intuitive yet conclusive results, such as increased suction capacity with reduced throat diameters [15]. Other findings included the lack of impact from varying throat lengths compared to other parameters.

Current research has shown that numerical models can accurately predict the performance of fertiliser injectors when compared to experimental results and provide insights into geometrical changes that improve performance. However, there is a gap in the literature regarding the application of venturi injectors for milk foaming purposes. Furthermore, no studies have been conducted on setting up a numerical model using saturated steam as a working fluid to create suction to a liquid and modelling heat transfer during this process.

2.7 Summary and Conclusion

From literature it is found that milk foam quality improves with temperature, with an optimum around 50 °C, especially when using milks with fat. This highlights the importance of heat transfer from steam to the suction fluid in defining the quality of the foam.
From the existing research, trends related to pressure drop and resistances due to friction and contraction have been established. Various numerical and physical experiments have been done for venturi injectors for agricultural applications. This research was done to investigate the flow field, pressure resistances, and suction pressure. However, the environment in which this occurs is substantially different than that of the venturi milk frother. While the existing research models single phase, single component flow, the venturi milk frother will require modelling of both multi-phase flow, in addition to heat and mass transfer between the phases. The effect multi-phase flow has on the single-phase expressions found in literature is described by an additional two-phase correction. However, this has not been validated numerically. Furthermore, there are additional pressure drops, resulting from condensation, for example, that are not analytically described. The effect of heat dissipation due to the milk mixing with the steam is dependent on how the two fluids mix. This makes it difficult to predict analytically and best to analyse numerically.
The trends seen from the analytical and empirical relations has also been seen in various research into venturi injectors. In those cases the goal was to use water to passively create suction and mix fertiliser within it.
In addition, a foundation has been made on suitable modelling choices for milk. Milk will be modelled as water in this research as this allows the goals to be met without adding additional complexity to the model.
Multiphase flow can be modelled in various ways, with the Eulerian method being more suitable for the venturi injector application. This models the two phases of fluids together with a boiling/condensation model to capture the change in phase between water and vapour. Furthermore, two eddy viscosity models can be used to close the Reynolds averaged conservation equations, with the SST model being more suited due to the influence of the boundary layer in such small geometries.

3 Methodology

In this research, both an experimental model and numerical model were set up and tested. The experiments serve as a reference point in calibrating and evaluating numerical models.

3.1 Experimental Methodology

To establish a benchmark for validating and comparing the CFD results, two experiments were conducted at Versuni in Drachten.
The first experiment was designed to determine the value of one unknown parameter in the boiling/condensation model: the interactive length scale. This length can be interpreted as the mean bubble size of the dispersed phase, which is an important characteristic for the heat and therefore, mass transfer between the two phases. The second experiment aimed to replicate normal operating conditions for the venturi-driven milk foamer.

3.1.1 Experiment 1 Setup - Bubble Size Tuning

The first experiment is designed to tune the interactive length scale, which affects the rate of heat and mass exchange. For example, a smaller length scale leads to an increase in evaporation in the neck and therefore a larger pressure drop from inlet to neck without increasing the power input to the system. If the power of the larger bubble size is increased to match the inlet pressure, the neck pressure is lower than that of the smaller bubble size. Knowing this, a combination of power input and bubble size is made to match the numerical results of pressure in the inlet and neck to those of an experiment.
To achieve this, saturated steam is pumped through the geometry. Using the pressure drop between the inlet and the neck, the interactive length scale is tuned. This is done by pumping water at a constant rate through a heater of a specific power and then the geometry. Pressure and temperature are measured before the venturi neck. These results give the same information as the saturation temperature is known for the given pressure. Both are measured to ensure that the results of the other can be trusted. Temperature is measured using a Type K thermocouple. Pressure is again measured in the neck. Lastly, the temperature is measured at the outlet. This measurement is expected to yield the saturation temperature at ambient pressure. After the outlet, an expansion tube is included. This is expanded so that there is little pressure loss. The tube is included to ensure the surrounding equipment does not get wet.
The pump is set to a mass flow of 0.25 g/s. The heater power is varied between three power settings 306.25 W, 525 W and 700 W. This gives three steam qualities. All measurements are repeated twice, and a third time if there is any difference in the results. The experimental setup is shown in Figure 3.1, with a close up of the venturi geometry in Figure 3.2. The pump is seen in Figure 3.3.

3.1.2 Experiment 2 Setup - Normal Use

The second experiment is similar to the first, with the addition of suction water and a downstream temperature measurement. The temperature measurement is made with a Type K thermocouple in the expansion tube. This is done to determine the mixture temperature. This temperature sensor is included as the temperature sensor right after the diffuser is influenced by how the two fluids mix. As seen from the flow field of the single phase water model in Figure 5.3, the working fluid is deflected to the upper half of the geometry, and the suction fluid is in the lower half. In the case of the experiment, it would mean that the temperature sensor at this point in the geometry will measure one of the two fluids, not a mixture of the two. As the temperature sensor is at the top of the geometry, it will measure the steam temperature. Therefore, a second measurement is made downstream. To ensure that the downstream temperature sensor captures the mixture of fluids, the thermocouple is placed along the bottom of the tube.

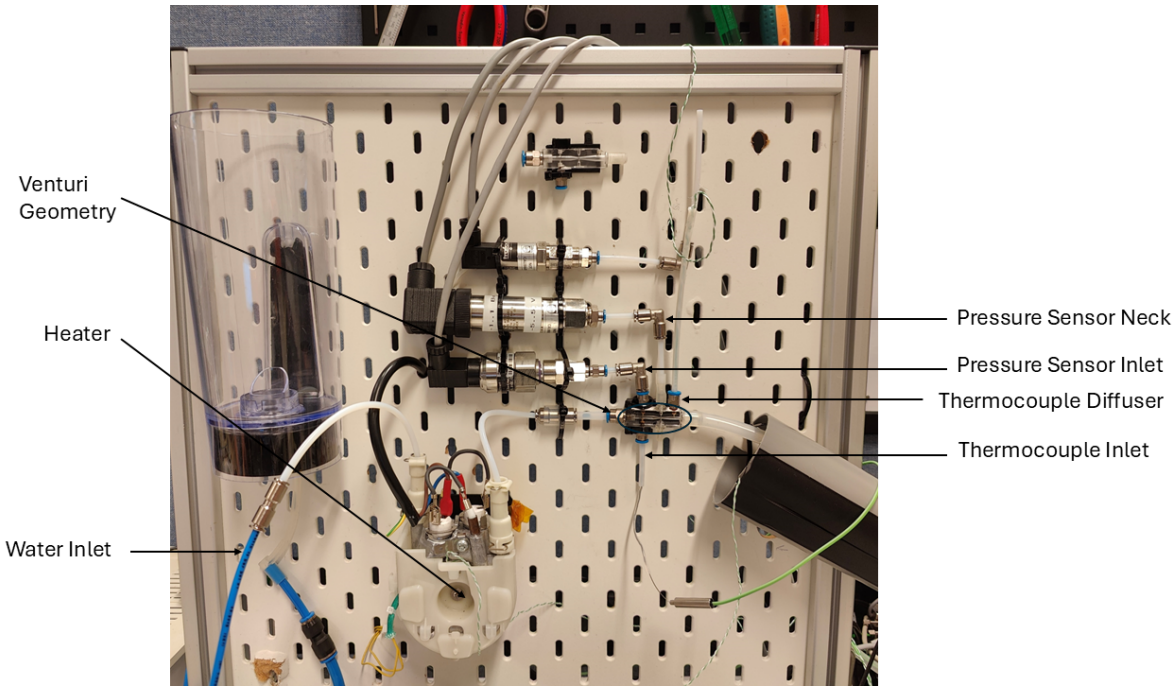

Figure 3.1: Experimental Setup Experiment 1.

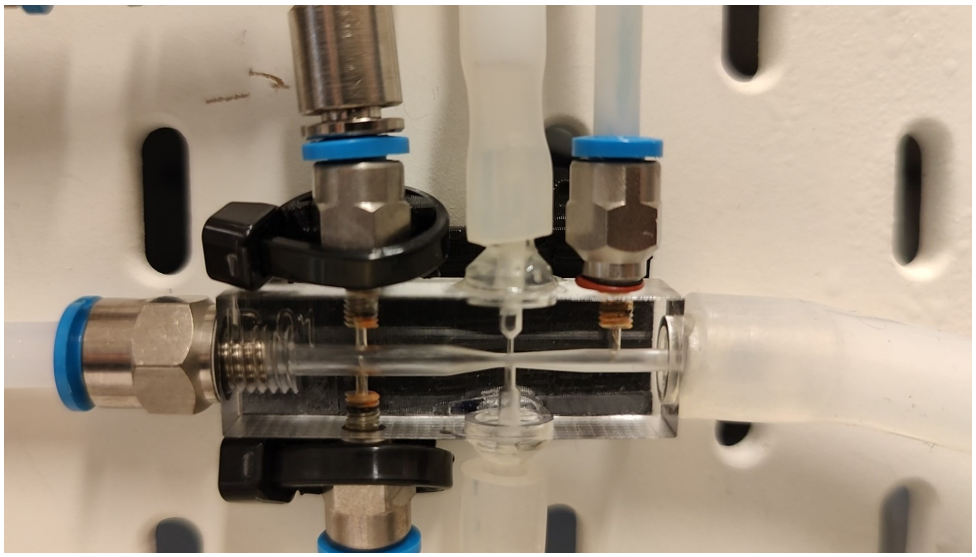

Figure 3.2: Experimental Venturi Geometry Close Up.

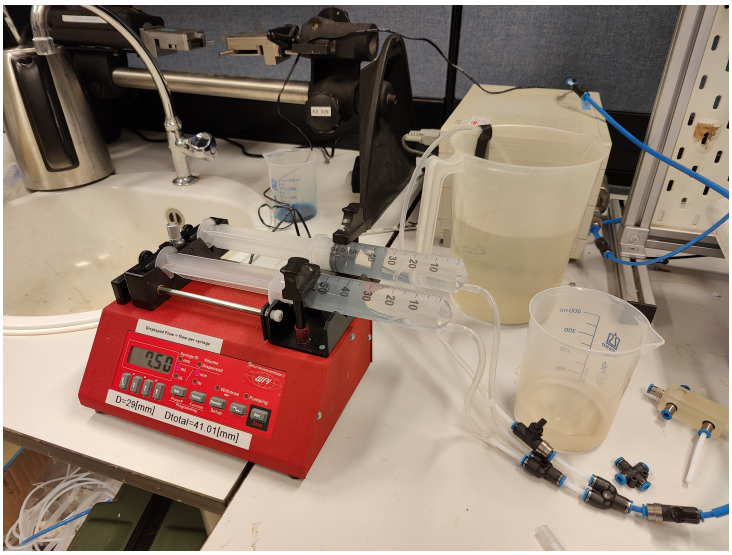

Figure 3.3: Experimental Pump.

The suction mass flow is measured by measuring the mass of the water reservoir over time. Lastly, the temperature of the water reservoir is also measured with another Type K thermocouple. Due to a limit on measurement logging, the downstream temperature and reservoir temperatures are read manually and not logged. This experiment is done with a mass flow of 0.25 g/s, for a range of five heater powers: 306.25 W, 437.5 W, 525 W, 612.5 W and 700 W. The experimental setup is shown in Figure 3.4. With the downstream thermocouple shown in Figure 3.5. The list of materials for both experiments are found in Appendix D.

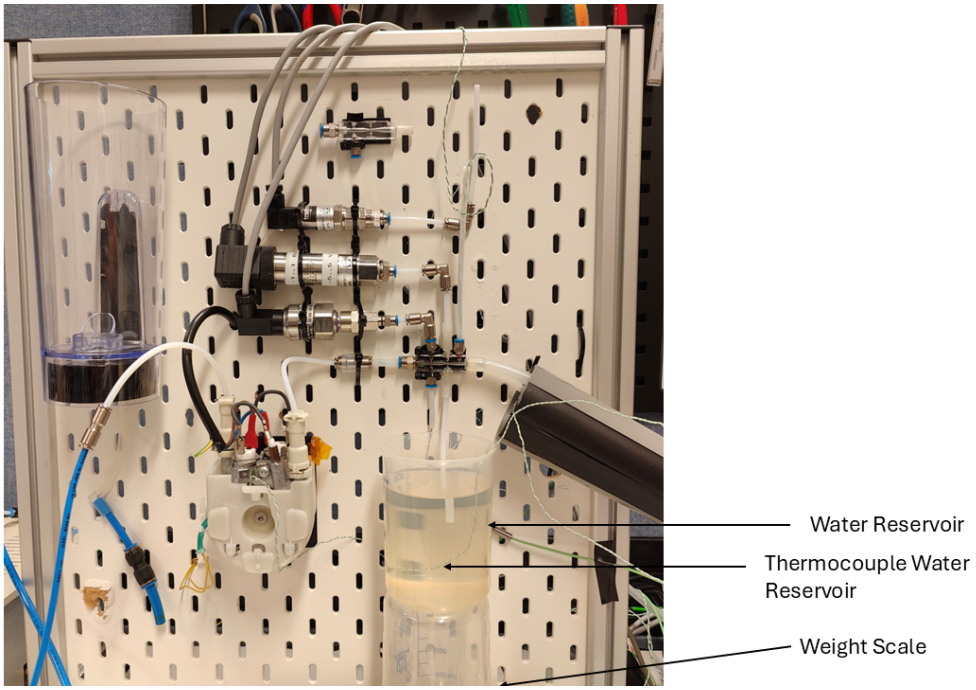

Figure 3.4: Experimental Setup Experiment 2.

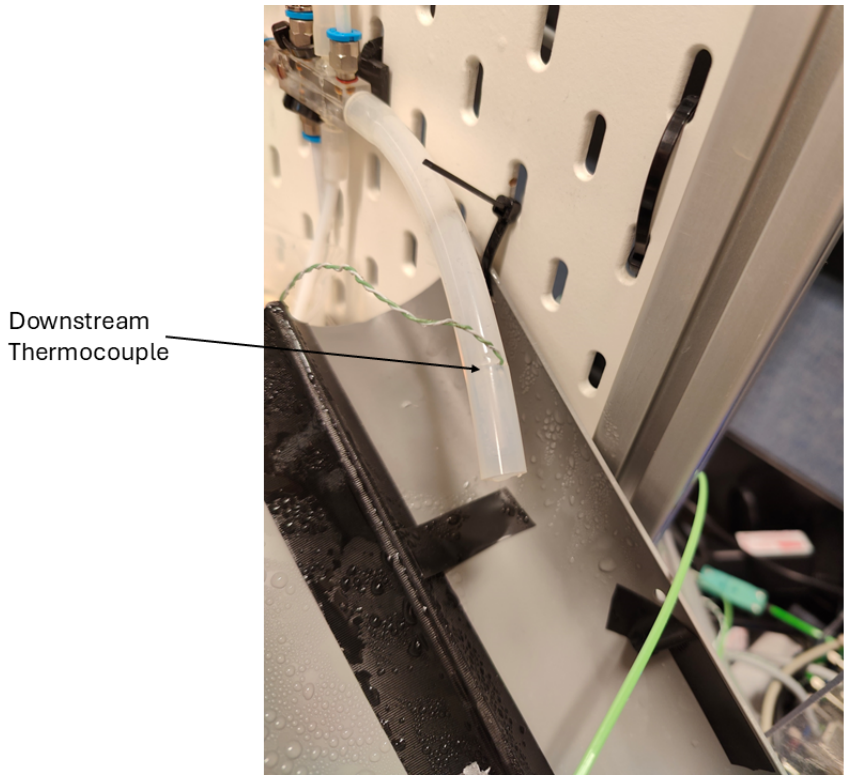

Figure 3.5: Downstream Temperature Measurement.

3.2 Numerical Methodology

The numerical model is constructed by first simulating the individual components of physics and then combining them into one comprehensive model to compare with experimental results. Doing this allows for a better understanding of where any possible differences in the latter research originate.

3.2.1 Numerical Set-Up

The numerical model is built using the commercial software Siemens Simcenter Star CCM+. To simulate the multiphase nature of the flow, the Eulerian multiphase model is employed. This solves the conservation equations discussed in subsubsection 2.5.2 for both phases. Additionally, a boiling/condensation model is incorporated to simulate the heat and mass transfer between the two phases using the theory discussed in subsubsection 2.2.3. Furthermore, all simulations are assumed to be adiabatic, meaning there is no heat exchange with the surroundings. Both water and steam use the state model of IAPWS-IF97 for their thermodynamic properties. The spatial discretisation is done using a second-order upwind method, while the temporal discretisation is done using a first order implicit Euler scheme, with a time step of 1e-3 s. The result is run sufficiently long to reach a steady state solution. Despite the expectation that the SST turbulence model would perform better for the small geometries being modelled [36], due to the reported advantages of k-ω model within the boundary layers while under adverse pressure gradients [9, 37], the RANS equations in subsubsection 2.5.2 are closed using the k-ϵ model due to the findings in subsection 5.2. The k$-\epsilon$ equations are solved for the mixture not for each phase, using mixture properties and velocities. The base size of the mesh is chosen to be 0.1 mm. A mesh refinement check is performed when necessary in section 5.

3.2.2 Static Pressure Drop

As discussed in subsubsection 2.3.1 the pressure drop between the inlet and neck is caused by an increase in the velocity due to the reduction in cross-sectional area, as well as total pressure resistances such as friction and contraction resistance. To investigate the relative contribution of each component to the static pressure drop, both a numerical calculation and semi-empirical calculation using the relations in subsubsection 2.3.1 is made.

The arbitrary venturi tunnel used in this research is depicted in Figure 3.6. For modelling purposes, only half of the tunnel was simulated, as this suffices to capture pressure resistances up to the center of the neck. To further reduce computational demands, geometry is modelled axisymmetrically.

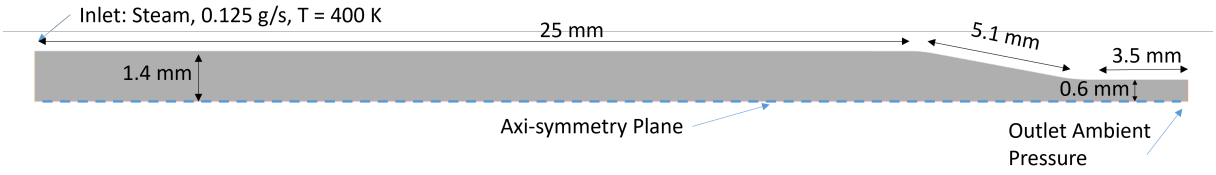

Figure 3.6: Venturi Tunnel Pressure Resistances.

This venturi tunnel model features an initial diameter of 2.8 mm, which constricts to a diameter of 1.2 mm via a bevelled wall. The length of the inlet tube and the neck are set at 25 mm and 3.5 mm, respectively. For this simulation, single phase steam at 0.25 g/s is used. This ensures the high velocity characteristic of the venturi injector are modelled. The outlet pressure is defined as ambient pressure (zero gauge pressure).

3.2.3 Suction of Fluid

To validate the ability to model suction, a numerical model is compared to an experiment from literature. This data comes from agricultural research where water is used to apply suction to fertiliser. This is modelled as a single phase water-water system as done in the literature [35]. Figure 3.7 shows the experimental geometry and its dimensions.. The inlet and outlet contraction angles α and β are 22^o and 7^o, which is more aggressive than the 10.5^o and 3.5^o in the geometry used to test the venturi driven milk foamer. The experiment measures the suction and outlet mass flows for a range of pressure drops. This is done by maintaining a constant inlet pressure of 0.1 MPa and varying the outlet pressure between zero and 0.05 MPa. The suction tube inlet is at ambient pressure.

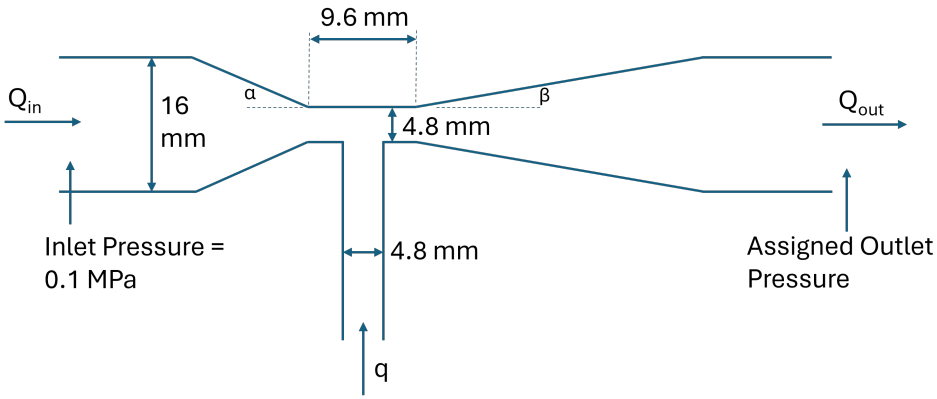

Figure 3.7: Experimental Geometry from Literature [35].

The CFD model is configured to replicate the experiment as closely as possible. The fluid is one phase and modelled as incompressible water. The inlet is defined as a stagnation inlet with a prescribed pressure of 0.1 MPa. Similarly, the suction inlet is defined as a stagnation inlet at ambient pressure. For both of these stagnation inlets, a reservoir is attached. This ensures that inlet effects of the stagnation inlet are not impacting the results. The outlet is a pressure outlet for which the pressure can be varied between zero Pa (ambient) and 0.05 MPa. The mesh is scaled by a factor 5 to match the larger geometry.

3.2.4 Multiphase Simulation

The goal of this phase of the research is to establish a multiphase simulation that accurately captures the thermodynamic physics which takes place within the venturi driven milk foamer. The input flow is saturated steam, which means that it is partially water and partially steam. It is not possible to model this state directly in Star CCM+ [9]. However, it can be done by modelling both water and steam. The combination of the two will give the saturated steam. Combined quantities like temperature and enthalpy are mass averaged. This is done by using the independent quantities and multiplying them by their respective mass fraction in each cell. These results can be validated using thermodynamic steam tables.
As mentioned, the Eulerian Multiphase model will be used, with a boiling/condensation model to capture the transfer of mass and energy between the two phases. In all simulations the outlet is always set to ambient pressure. To ensure that the rate of heat transfer is modelled correctly, the Nusselt number of each regime is calculated using Equation (2.5) to Equation (2.9). This is done in each cell and defined as a field function. An example of the results of these calculations for a plane in the inlet can be seen in Table 3.1.

Table 3.1: Nusselt Numbers.

Nusselt Number	
Continuous Water	4.7
Dispersed Steam	3.2
Continuous Steam	6.6
Dispersed Water	5.4
Intermediate Water	11.4

For such a milk injector it is required for the thermodynamic state to be within the vapour dome before entering the neck, and to have control over the mass fraction of steam entering the venturi neck. This is not possible using a standard mass flow inlet, as specifying the temperature would result in a phase change due to differences between the inlet temperature and saturation temperature. The pressure at the inlet is calculated during the simulation, therefore, the temperature has to be iteratively chosen to ensure the bulk fluid is within the vapour dome. In practice, this is difficult to do, therefore an alternative is necessary. To better control the position of the bulk fluid within the vapour dome, it would be advantageous to set the enthalpy as a boundary condition. Unfortunately, this is not directly possible. As an alternative approach, the model can be modified such that the inlet condition is always known and then increase the energy to achieve the desired enthalpy. To accomplish this, the inlet condition is set to be fully water at a temperature below the saturation temperature at ambient pressure, in this case 370 K. A volumetric heat source is then added to increase the energy of the system, such as seen in Figure 3.8. This setup can be seen as an extended inlet condition.

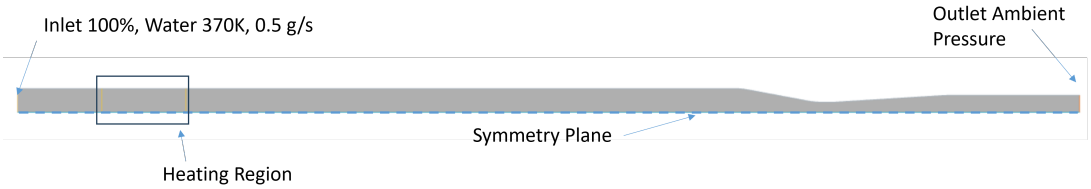

Figure 3.8: Volumetric Heater Configuration.

3.2.5 Final Numerical Model

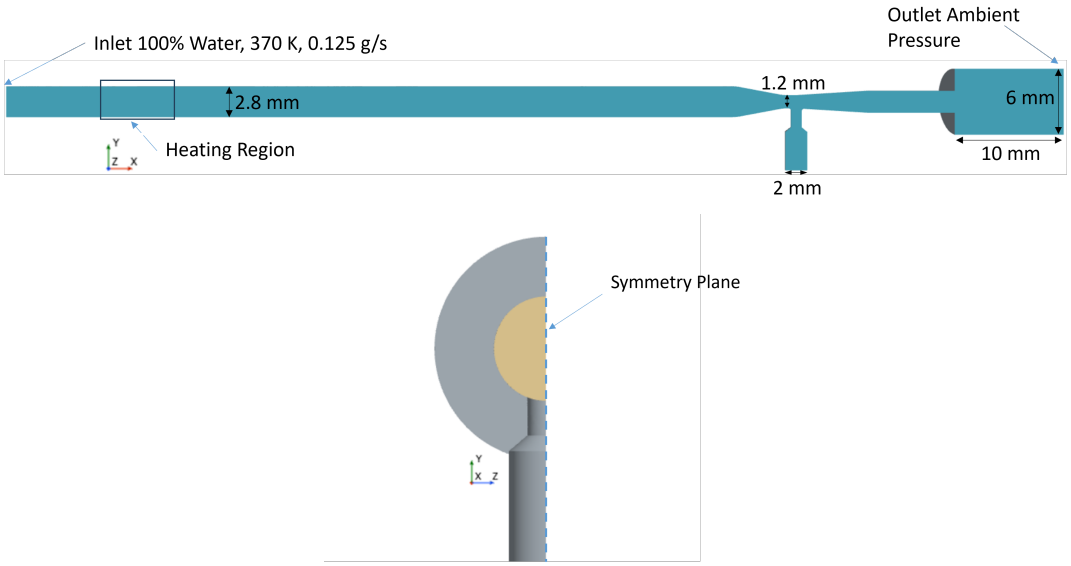

Figure 3.9: Geometry of Numerical Model Simulating the First Experiment.

To ensure the numerical model is modelling the rate of phase change accurately, the interactive length scale is tuned to the results of the first experiment. This model uses only saturated steam through the geometry. The experiment is numerically recreated with the geometry seen in Figure 3.9. The geometry is the same as that in earlier parts of the paper, but expanded to include the first section of outlet and suction tube. The suction tube is closed off at its end. Due to the nature of the geometry, the model is now 3D. The inlet is defined as a mass flow inlet with water entering with a mass flow of 0.125 g/s and temperature of 370 K. Water is heated with a volumetric heater to add energy to the system and create saturated steam of a given mass fraction. The inlet mass flow rate is half of that in the experiment, as only half the geometry is modelled. A symmetry plane is used to split the geometry as seen in Figure 3.9. The outlet is defined as a pressure outlet, at ambient pressure.

Similarly, the geometry of the final numerical model replicates that of the second experiment. The length of widened downstream domain is 10 cm to ensure that the temperature can be monitored downstream and compared to the experiment. Similarly, the length of the suction tube is also the same as the experiment at 10 cm, ensuring that the frictional resistance between the neck and the reservoir is simulated. The suction inlet is defined as a stagnation inlet, with ambient pressure. The rest of the simulation remains unchanged from the numerical model used to tune the interactive length scale. The geometry can be seen in Figure 3.10.

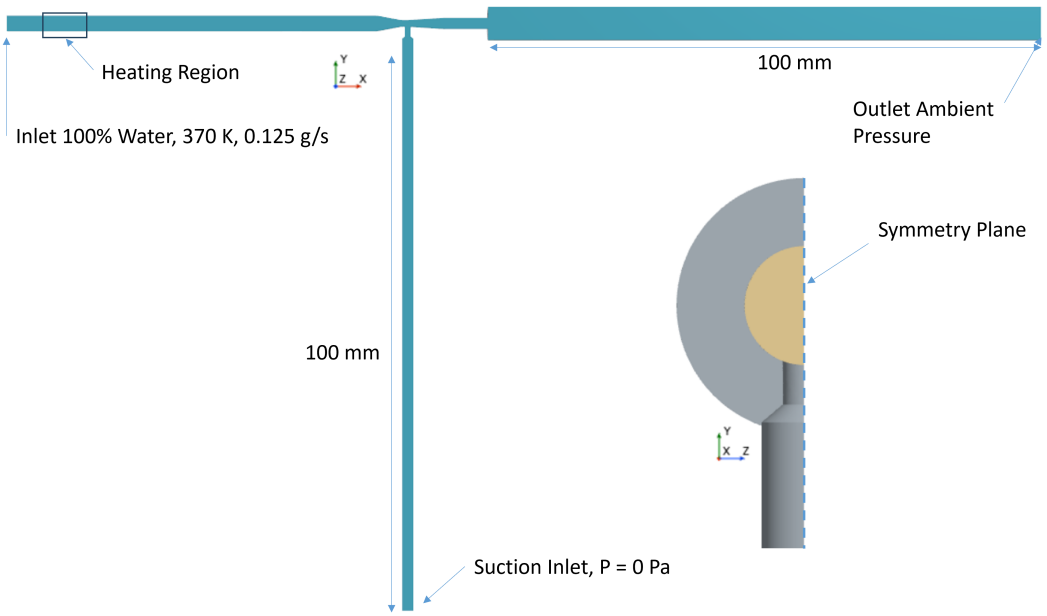

Figure 3.10: Geometry of Numerical Model Simulating the Second Experiment.

As the power input for the heater is not known for points not simulated in the first experiment, the correlation between the specific power of the simulation and the experimental input power is plot, as seen in Figure 3.11. This allows the heater power to be defined for additional points. Together with the mass flow rate, the power input defines the inlet condition. Using this range of inlet conditions, the experimental measurements can be calculated numerically.

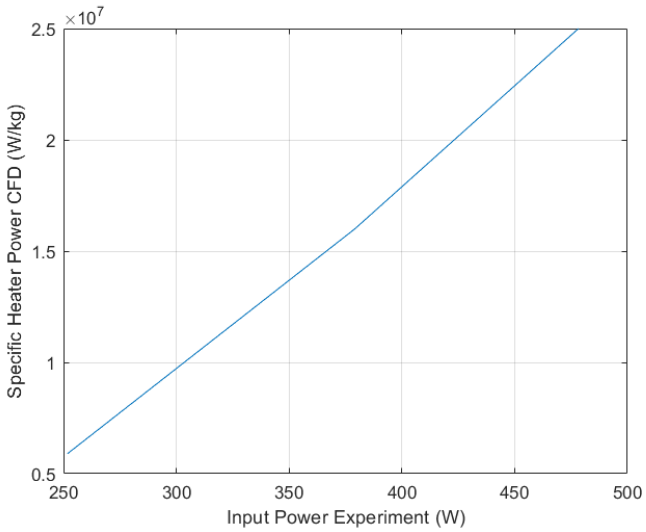

Figure 3.11: Correlation Between Experimental Power Input and Numerical Heater Power Input.

4 Experimental Results

For all measurements, the experiment is carried out long enough to reach a steady state solution. The data is truncated to only include the steady state region. Over this region an average is taken. All measurements are completed twice to ensure that the result is independent of external factors. If any discrepancies arise, a third measurement would be taken.

4.1 Experiment 1 Results - Bubble Size Tuning

The experimental results are presented in Table 4.1. It is seen that temperatures measured at locations where pressure is also recorded or known, are close to the saturation temperatures, allowing the the pressure measurements to be trusted. At the outlet, the expansion tube may add some additional resistance as the outlet temperature is higher than the saturation temperature at ambient pressure. The additional resistance is marginal and not sufficient to justify expanding the geometry to include it.
The steam quality is determined by defining the enthalpy of the fluid using the energy input from the heater with a pure convection loss estimated and deducted from the power input. Together with the inlet pressure and this enthalpy, the steam quality is determined from steam tables. Unfortunately, this method does not give an accurate estimate of the steam quality. The estimates of losses are not sufficient, leading to an estimated steam quality that is higher than it is in reality. This could be tested by calculating the static pressure drop due to the change in area for a range of mass fractions, as seen in Figure 4.1. Since this calculation neglects additional resistance, it represents a minimum static pressure drop. The calculated pressure drops are larger than those measured, indicating that the estimated mass fraction is too high. Therefore, the measurements will be denoted using the power input to the heater.

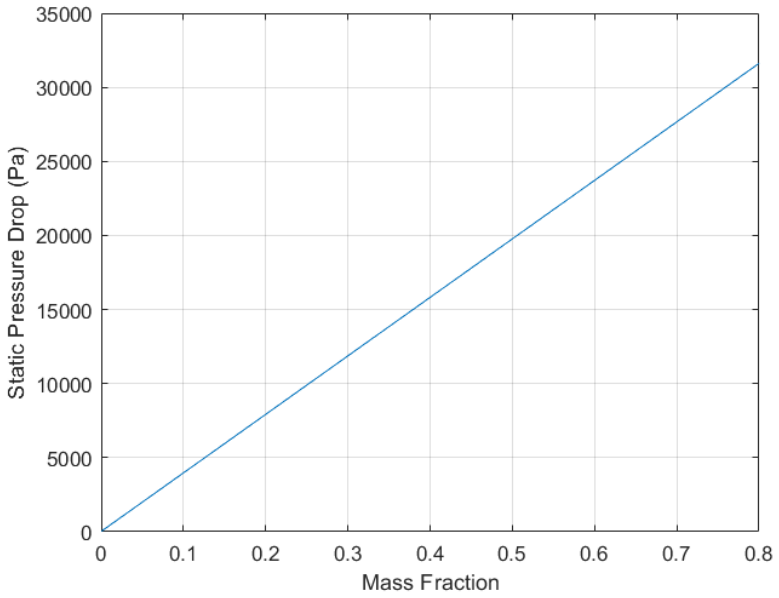

Figure 4.1: Minimum Static Pressure Drop Due to Change in Area for Range of Mass Fractions.

4.2 Experiment 2 Results - Normal Use

The results of experiment 2 are presented in Table 4.2 and Table 4.3.
As with experiment 1, the saturation temperature is calculated using the pressure and the steam tables. These again matched the measured temperatures. In all cases, the reservoir temperature

Table 4.1: Experiment 1 Results.

Heater Power (W)	Pressure Inlet (Pa)	Calculated Saturation Temperature (°C)	Inlet Temperature (°C)	Throat Pressure (Pa)	Outlet Temperature (°C)
306.25	2210	100.6	100.7	-1840	100.3
525	9590	102.5	102.7	-11370	100.2
700	19800	105.1	105.2	-21780	99.9

is 22 °C. The suction mass flow does not increase linearly with the increase in mass fraction but tapers off at higher power inputs.
When comparing the results of the first, third and fifth measurement to those of experiment 1 (without joining flow), it is seen that while the pressure drop remains similar, the latter two neck pressures are higher for experiment 2 with joining flow. A higher neck pressure is caused by a lower pressure gain between the neck and the outlet. This has two possible explanations; the first being that additional condensation in the outlet region causes additional friction resistance, which increases diffuser pressure and subsequently raises the neck pressure. However, the findings up to this point have shown that the frictional resistance does not play such a significant role as that of the dynamic pressure gain. Therefore, it is concluded that change of pressure in the neck is caused by a smaller reduction in velocity from neck to outlet. How the pressure in the neck is affected by a joining flow will be further investigated using the numerical model to gain additional insight.

Table 4.2: Experiment 2 Pressure and Mass Flow Results.

Heater Power (W)	Pressure Inlet (Pa)	Throat Pressure (Pa)	Suction Mass Flow (g/s)	Mass Flow Ratio Q_s/Q_{out}
306.25	2250	-1940	0.428	0.631
437.5	8250	-4090	0.996	0.799
525	14550	-6320	1.318	0.841
612.5	23150	-8640	1.551	0.861
700	28090	-9940	1.652	0.869

Table 4.3: Experiment 2 Temperature Results.

Calculated Saturation Temperature (°C)	Inlet Temperature (°C)	Outlet Temperature (°C)	Downstream Temperature (°C)
100.6	100.7	100.0	99.3
102.2	102.4	94.9	90.0
103.8	104.0	94.4	89.0
105.8	106.1	96.2	91.0
107.0	107.2	96.6	92.0

During the experiment, two possible scenarios were experienced: one with partly condensed fluid in the diffuser and another with fully condensed fluid. The latter is noticeably quieter due to the lower velocity flow. Interestingly, the second situation also has a higher suction mass flow, leading to a further fall in the mixture temperature. This situation was only encountered

in one measurement and not reproduced. The reason the suction pressure increases due to condensation in the diffuser is due to the large decrease in velocity during condensation. This effect is stronger than the contraction due to the phase change. As the mass flow is constant, $\rho \cdot u$ is constant. This means the dynamic pressure,

$$p_d = \frac{1}{2}\rho u^2 \tag{4.1}$$

can be written as,

$$p_d = \frac{1}{2}\mathrm{C} \cdot u \tag{4.2}$$

where C is the constant. This means that the dynamic pressure decreases for the case of condensation more than a case without condensation. This therefore means that the static pressure increase must also be larger. As the pressure is calculated from the outlet and the loss between the diffuser and the outlet is only due to frictional losses (which have been shown to be a smaller order of magnitude), the static pressure in the neck must be lower for the case of condensation in the diffuser.

5 Numerical Model Results

In this section the results of the numerical model are discussed. This includes both the individual physics modelling, the tuning of the model and the comparison of the CFD model to the experimental results.

5.1 Static Pressure Drop

A comparison of the velocities calculated by hand and those calculated by Star CCM + is seen in Table 5.1. The hand calculations for velocity are made using the known mass flow rate, fluid density and area,

$$u = \frac{\dot{m}}{\rho A}. \tag{5.1}$$

The velocities of the CFD model are higher due to the decreased effective area caused by the existence of a boundary layer. As the velocity is above a Mach number of 0.3, the steam state model IAPWS-IF97 is used to ensure that any compressible effects are accounted for. This further increases the difference between the velocities in the neck.

Table 5.1: Velocity of Steam in Inlet and Neck.

Velocity	Hand Calculation	Star CCM+
Inlet	34.10 m/s	34.30 m/s
Neck	185.66 m/s	205.10 m/s

Figure 5.1: Velocity Field for Single-Phase Steam Passing Through a Nozzle.

Using the relations in subsubsection 2.3.1, the pressure resistances due to friction and contraction are calculated. Additionally, the dynamic pressure rise due to the change in area is calculated using the Bernoulli principle. As the velocity is above Mach 0.3, it cannot be assumed that the fluid is incompressible, which means the semi-empirical pressure calculation will deviate from reality. However, this method still provides a quick estimate of the order of magnitude for each component of the pressure drop. Combined, these will give a static pressure drop from inlet to neck, which is shown in Table 5.2 compared to the numerical results. To be able to model the friction and contraction separately in CFD, one run is done with slip walls to capture only the contraction, and a second run is done with no slip walls to capture both friction losses as well as the same contraction resistance. The results are subtracted from each other to give the friction losses. It should be noted that friction on the contracting section of the wall must be included to model the separation that creates the contraction resistance. Without it, there are little to no contraction losses.
Static pressure in the neck is crucial, as it defines the suction pressure which powers the injector effect. The pressure in the neck is defined by what occurs after the neck, as all pressures are defined from the known pressure at the outlet. The pressure drop calculated here therefore defines the inlet pressure. The inlet pressure is important as it defines the thermodynamic situation at the inlet. In this case, there is a 16% difference in the total static pressure drop between the semi-empirical hand calculations and the Star CCM+ calculation. The majority

Table 5.2: Pressure Difference Between Neck and Inlet.

Pressure Difference	Hand Calculation	Star CCM+
Friction Resistance	1080 Pa	560 Pa
Contraction Resistance	265 Pa	560 Pa
Dynamic Pressure Gain	10160 Pa	12520 Pa
Total Static Pressure Drop	11510 Pa	13640 Pa

of this difference comes from the increase in velocity in the neck leading to a larger decrease in static pressure. As mentioned, this difference originates from the difference in effective area due to the existence of a boundary layer and the fluid being compressible. The semi-empirical relations do not account for compressible flow, therefore, if an incompressible gas is modelled, the difference between the results drops to 8%.
This provides insight into the order of magnitude of the various pressure contributions. Now that the pressures throughout the domain are better understood, the suction mass flow that this creates can be modelled.

5.2 Suction of Fluid

The results of the experiment from literature are shown in Table 5.3. Important for venturi injectors is the ratio of the two fluids; this is therefore shown in the last column. The ratio is defined as the suction mass flow divided by the outlet mass flow.

Table 5.3: Experimental Data for Suction/Outlet Volume Flow and Ratio at Varying Outlet Pressures.

Outlet Pressure (MPa)	Suction Mass Flow (L/h)	Outlet Mass Flow (L/h)	Ratio $x10^{-2}$
0.00	114.48	1155.43	9.91
0.01	93.99	1077.74	8.72
0.02	87.02	1060.29	8.21
0.03	66.63	1023.53	6.51
0.04	47.36	999.14	4.74
0.05	15.78	984.12	1.6

The expectation was that the SST turbulence model would provide more accurate results over alternatives such as the k-ϵ model, due to its ability to use the k-ω to capture wall effects and blend into k-ϵ in the bulk flow. Unfortunately, in this case, when using the SST turbulence model, the resulting suction volume flow is transient and regularly encounters back-flow down the suction pipe. Furthermore, when an average is taken over time, the result is heavily underpredicted, with around half the expected suction mass flow. This is not encountered when the k-ϵ model is used. This converges to a steady-state solution close to the result of the experiment. The convergence plot of suction mass flow can be seen in Appendix E.1. Mesh dependency has been tested by halving the mesh size, this yielded a 0.6% difference as shown in Appendix F.1. The results are therefore deemed independent of the mesh.

For this application, where the amount of suction mass flow is a quantity that should be predicted accurately, the k-ϵ model appears to be more effective in modelling it. This will

likely come with losses elsewhere in the domain; however, it is the best option available without investing in additional computational power and time. It is possible that a more detailed turbulence model or Large Eddy Simulation is required to sufficiently model the mixing of the two fluids and, therefore, the suction mass flow. However, the additional computational resources that come with this mean it is not a suitable option. Therefore, the k-ϵ model is used, as it sufficiently models the behaviour of suction mass flow.
The results of the simulation volume flow ratio compared to that of the experiment is depicted in Figure 5.2. The complete results are shown in Appendix B. Notably, the simulation can accurately model the ratio of suction fluid to total outlet fluid to within a 6.5% for all but the highest outlet pressure. The reason for the difference at the last measurement point is unknown. However, as the results for the remaining 5 points shows good correlation with the experiments, and the ratio of suction to total flow expected in the venturi milk frother is not as low as this last measurement, the model is concluded to be sufficient to move on to the next phase. The flow field for an outlet pressure of zero Pa is shown in Figure 5.3.

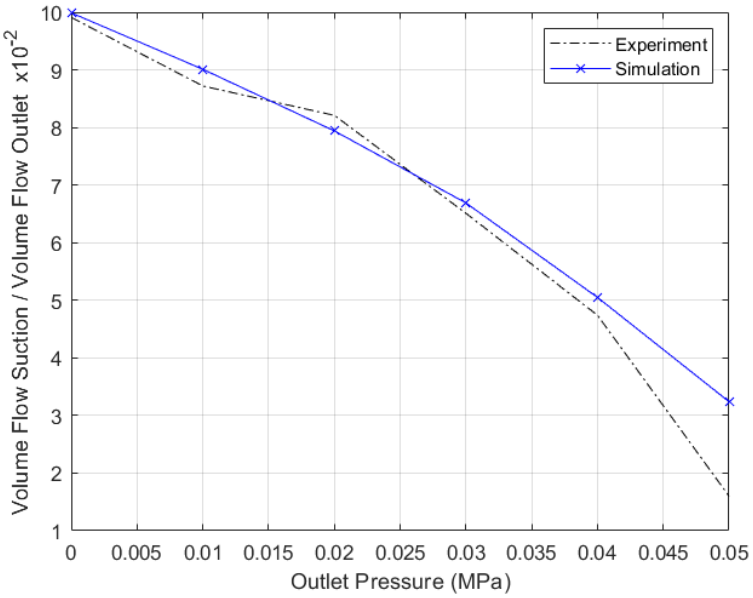

Figure 5.2: Ratio of Suction Water to Outlet Water.

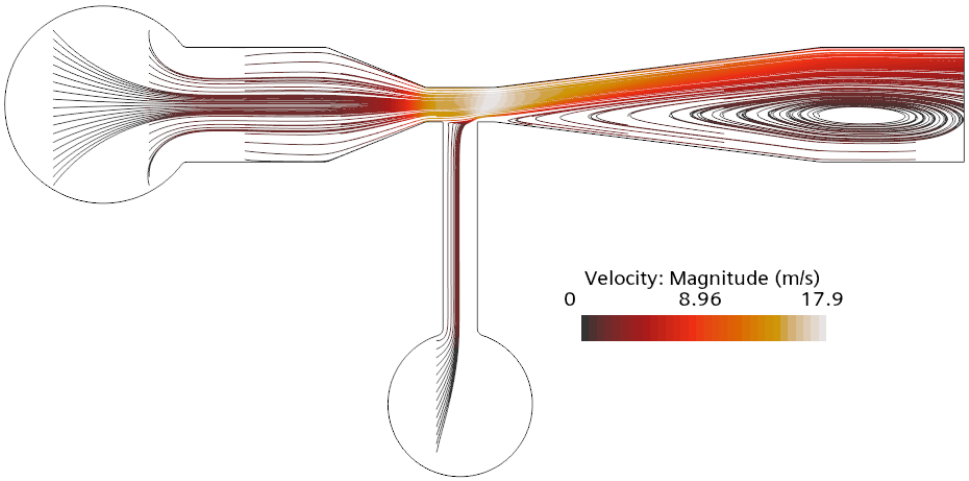

Figure 5.3: Suction Experiment from Literature Flow Field.

5.3 Multiphase Simulation

Using the setup discussed in subsubsection 3.2.4, the fluid thermodynamic state can be within the vapour dome. The resulting volume fraction is seen in Figure 5.4. In Figure 5.4 the mass fraction is also shown, as this gives a better representation of the distribution in the high volume fractions of steam. Furthermore, it is the quantity used in thermodynamics to describe the quality of the steam. To ensure that the temperature profile is as uniform as possible, the walls before and within the heater are given a slip condition. This gives the velocity a uniform profile and therefore, the temperature a uniform profile. If this is not done, the low velocity flow close to the walls is heated excessively as seen in Figure 5.5.

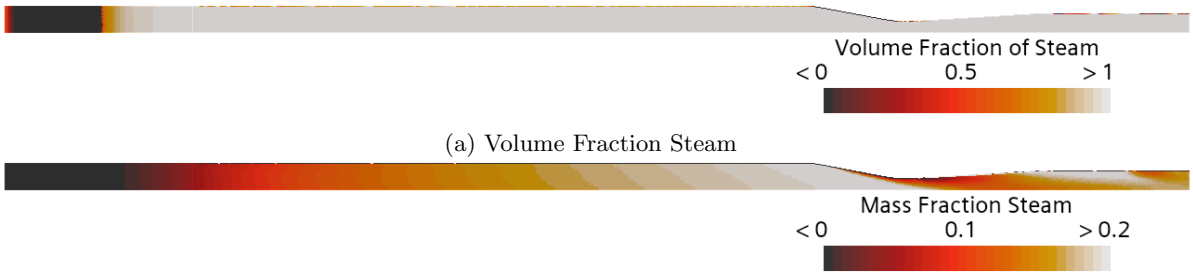

(a) Volume Fraction Steam

(b) Mass Fraction Steam

Figure 5.4: Multiphase Fractions of Steam.

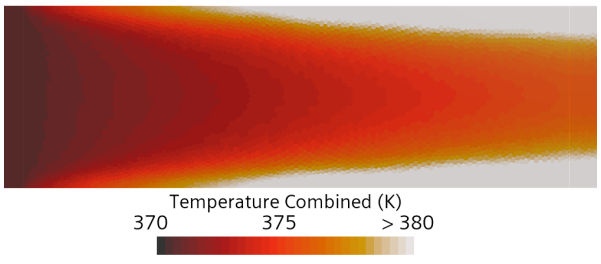

(a) Heating Region With No-Slip Walls

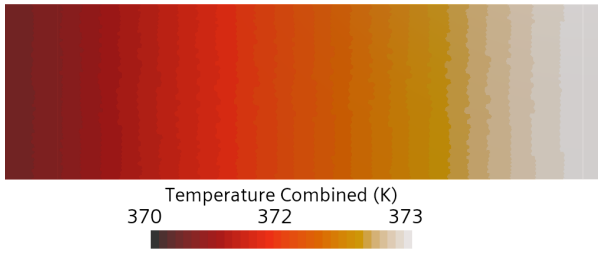

(b) Heating Region With Slip Walls

Figure 5.5: Temperature Profiles Heating Region.

As mentioned, this setup should be seen as an extension of the inlet condition, such that the steam quality of the fluid before the neck can be defined. The power of the heating region determines the amount of energy put into the system and subsequently how far the fluid is pushed into the vapour dome. For this example, the result is shown in Figure 5.6.

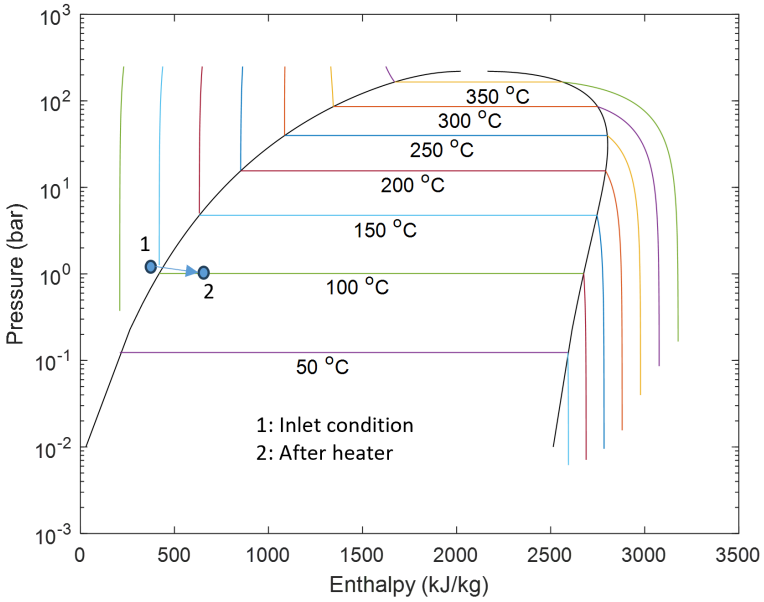

Figure 5.6: Effect of Heater on Fluid Enthalpy.

As discussed in subsubsection 2.2.3, the Nusselt number for the gas side of the interface is not defined for the intermediate region. To investigate this uncertainty, a sensitivity analysis is performed by varying the value of the Nusselt number and examining the effect. Three calculations were done: one with the same Nusselt number as the liquid side, another with an order size smaller, and a third with an order size larger. It was seen that for the same point in the domain, the results tend to the same value regardless of the assigned Nusselt number to within 2%. Therefore, it is chosen to use the same Nusselt number as the liquid side of the interface going forward.

The results show that the total energy is constant along the domain, with a drop in pressure in the neck and a subsequent rise in the diffuser towards the ambient outlet. The drop in pressure is accompanied by an increase in the mass fraction and a decrease in the temperature as expected from the thermodynamic tables. However, these changes do not occur simultaneously, with the change in temperature and mass fraction occurring further downstream than the neck, in the outlet region. This leads to an error between temperature, pressure, and specific enthalpy when compared to the expectation from steam tables. It is important to note, that for each phase the temperature is solved using the total energy conservation equation. Using pressure and temperature, the Gibbs-free energy per phase is calculated according to the corresponding state functions [9]. Using the Gibbs-free energy, the specific enthalpy is calculated. Therefore, in Star CCM+ the specific enthalpy is a function of pressure and temperature. It is therefore unusual that the temperature and specific enthalpy and the system pressure do not match as expected from the steam tables. To investigate these discrepancies, the specific enthalpy, temperature, and pressure of each phase after the heater are individually checked and compared with the expectation from the steam tables. The results are seen in Table 5.4. The results show that for steam, Star CCM+ accurately determines the set of three variables relative to each other. However, this is not the case for water, where the calculated specific enthalpy is too low. This discrepancy is caused by the water being at a temperature and pressure where it should be steam. Since the specific enthalpy is calculated in the water state model, the highest possible enthalpy (saturated water enthalpy) is assigned. This is also visualised using Figure 5.7. This results in a specific enthalpy that is being underpredicted. It is clear that this problem originates from the boiling model, as it is expected that this water

Table 5.4: Comparison of Calculated Temperature using Star CCM+ and Steam Table.

	Star CCM+	Steam Table Calculation
Static Pressure	285.8 Pa (Gauge)	
Specific Static Enthalpy Water	428.9 kJ/kg	
Temperature Water	102.3 °C	100.1 °C
Static Pressure	285.8 Pa (Gauge)	
Specific Static Enthalpy Steam	2791.9 kJ/kg	
Temperature Steam	159.3 °C	159.3 °C

should be steam. The only unknown in this model is the interactive length scale (mean bubble size). By reducing the bubble size, you increase the rate of evaporation of water into steam. This can be seen in Figure 5.8, where the temperature of the water is shown along the centre line of the tube after passing through the heater. The temperature of water decreases as the hot water evaporates to steam. This is also reflected in Figure 5.4b, where the mass fraction of steam increases further along the domain after the heater. This process does not occur instantaneously but occurs over a short period of time.

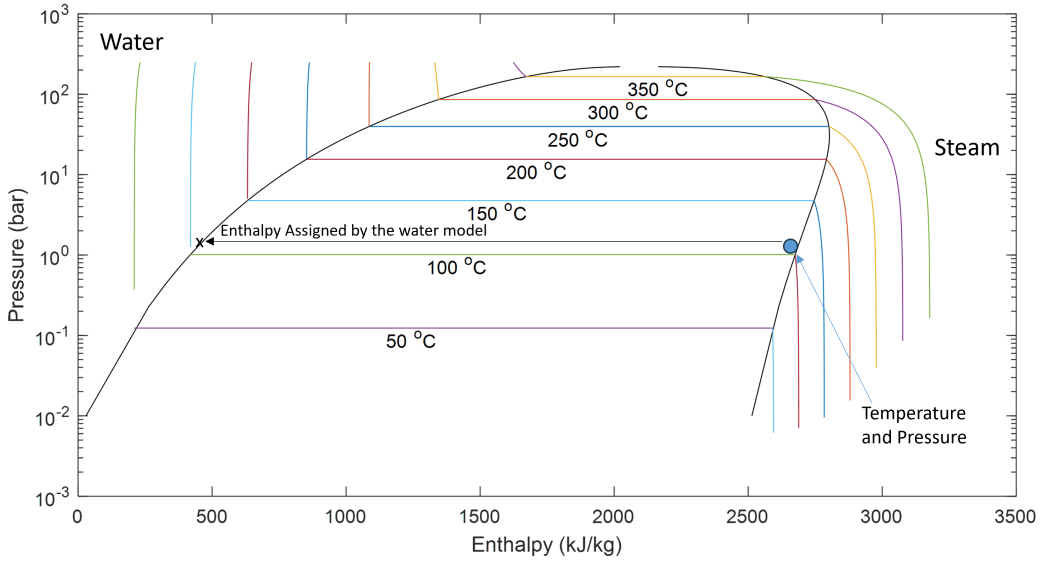

Figure 5.7: Enthalpy Calculation Overheated Water.

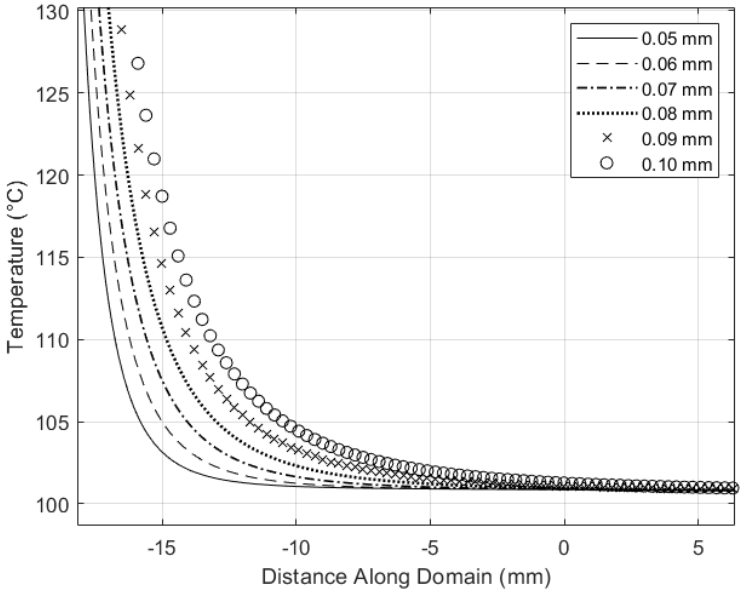

Figure 5.8: Temperature Drop for Varying Bubble Size.

As shown in Figure 5.8, increasing the bubble size slows down the rate of evaporation and prolongs the time it takes for the water temperature to reach its boiling point. In the case of a large bubble size the measurement is taken before the temperature has reached its boiling temperature, whereas with a smaller bubble size, it has reached the boiling temperature. Once this equilibrium has been reached the temperature, pressure and enthalpy match as expected and seen in Table 5.5. This behaviour is consistent with the equations that govern the heat transfer rate and the area over which heat transfer occurs. Both the heat transfer rate and the area increase by a decreasing length scale. The area is defined as an area density. Therefore, the area per volume of fluid. This is therefore a function of $\frac{1}{L}$. The heat transfer coefficient is a function of $\frac{\mathrm{Nu}}{L^{0.5}}$, where Nu is a function of $L^{0.5}$. Meaning a combined function of $\frac{1}{L^{0.5}}$.
The actual bubble size is unknown. From an initial estimation it is reduced from the 1 mm to 0.1 mm as the bubble size is visually an order size smaller than the 1.4 mm diameter neck as seen from the slow-motion video (a snapshot is shown in Appendix C).

Table 5.5: Comparison of Calculated Temperature using Star CCM+ and Steam Table.

	Star CCM+	Steam Table Calculation
Static Pressure	540.954 (Gauge)	
Specific Static Enthalpy Water	419.5 kJ/kg	
Temperature Water	101.1 °C	100.1 °C
Static Pressure	540.954 Pa (Gauge)	
Specific Static Enthalpy Steam	2675.9 kJ/kg	
Temperature Steam	100.3 °C	100.3 °C

The time dependency has consequences that impact the performance of the model, making it important that the interactive length scale is chosen appropriately. For example, the amount of evaporation that occurs in the neck due to the pressure drop affects the velocity and therefore also the pressure in the neck. To better estimate the interactive length scale, an experiment

with only saturated steam in the system is used to tune to CFD result to. It is essential to note that due to the phase change occurring over time, the specific enthalpy calculated by Star CCM+ will not always give an accurate reading. Therefore, the sum of total enthalpy is used to ensure energy conservation.

5.4 Complete Model

In this section, the physics is integrated to form a complete model that simulates the operation of a thermal venturi injector for milk foaming applications. It is important here to first tune the interactive length scale using the data from the first experiment as this defines the rate of phase change.

5.4.1 Bubble Size Tuning

By adjusting the power of the volumetric heater and the interactive length scale, the results of pressure at the inlet and neck can be tuned to that of the experimental results in subsection 4.1. An example of the pressure through the domain, at an inlet steam quality of 26%, is seen in Figure 5.9.

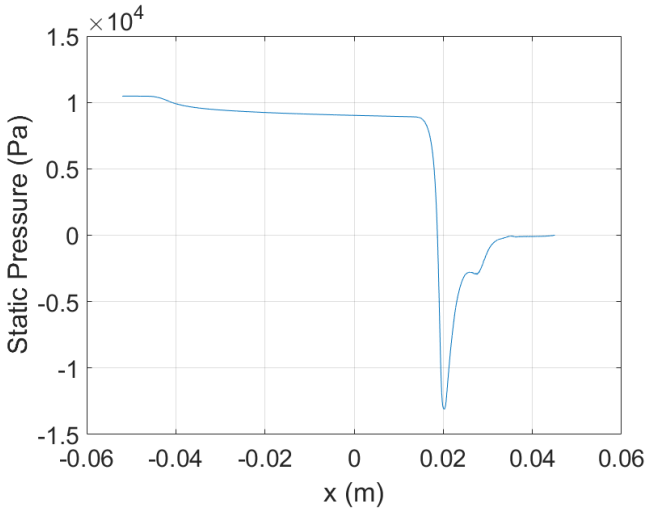

Figure 5.9: Pressure Drop Through the Domain During Bubble Size Tuning.

Varying the bubble size at the lowest of the three inlet steam qualities has significant influence on the neck pressure. Using a bubble size of 0.4 mm gives good agreement with the results at this steam quality, which is consistent with the estimated value of approximately 0.1 mm based on the slow-motion snapshot. At the highest inlet steam quality, the CFD deviates from the experimental results. Varying the bubble size in this regime has little effect, as seen by the results in Table 5.6. The bubble size is chosen such that it is best suited for the range of steam qualities, 0.4 mm. The resulting numerical pressure drops from inlet to neck as well as those from the experiment are seen in Table 5.7.

Table 5.6: Numerical Pressure Results for Two Different Bubble Sizes.

Bubble Size (mm)	Inlet Pressure (Pa)	Neck Pressure (Pa)
0.4	19640	-35650
0.1	19260	-32900

Table 5.7: Numerical Pressure Drop After Bubble Size Tuning.

Inlet Steam Quality (%)	Inlet Pressure Experiment (Pa)	Inlet Pressure CFD (Pa)	Neck Pressure Experiment (Pa)	Neck Pressure CFD (Pa)
8%	2210	2280	-1840	-1830
26%	9590	9120	-11370	-12190
47%	19790	19640	-21780	-35650

For comparison, the multiphase pressure drop discussed in subsubsection 2.3.1 is calculated and compared to the experimental and numerical results in Table 5.8. In this case, both the liquid and gas phases are turbulent, which means that the friction multiplier used is 20 (as specified in Table 2.1).

Table 5.8: Analytical Pressure Drop Compared to Experimental and Numerical Results.

Inlet Steam Quality (%)	Experimental Pressure Drop (Pa)	Numerical Pressure Drop (Pa)	Analytical Pressure Drop (Pa)
8%	4050	4110	3890
26%	20970	21310	14280
47%	41570	55290	29820

The analytical prediction underpredicts the pressure drop when compared to the numerical and experimental results as also seen in subsection 5.1. This discrepancy is attributed to differences in the neck area, due to the boundary layer and compressibility. At the lowest inlet steam quality the deviation is only 4%. However, this difference increases with higher steam qualities.

5.4.2 Pressure and Suction Mass Flow

Using the geometry depicted in Figure 3.10, the simulation passively injects water into the saturated steam mixture using the underpressure created in the neck. As cold water mixes with the saturated steam, it heats up while simultaneously condensing the steam. The extent of condensation depends on the amount of energy lost to the water, injecting more cold water leads to increased condensation and a colder mixture temperature. Similarly, as in the case of evaporation within the heater, condensation does not all occur instantaneously due to the heat transfer between phases.
The resulting suction mass flows and pressures are presented in Table 5.9 and Table 5.10, where they are compared to those from the Experiment 2. A visual representation of the ratio can be seen in Figure 5.10. The data reveals that across all input steam qualities, both the suction mass flow rate and therefore the mass flow ration are underpredicted. These simulations were run until their result was steady state, the convergence of pressure is shown in Appendix E.2.

To verify mesh independence, a check was carried out. This involved doubling the mesh density and inspecting any change in the result. In this case, the suction mass flow increased by only 0.2%. The same was done with the time step, resulting in a decrease in suction mass flow by 2.2%. The absolute results are presented in Appendix F.2. Given that this minimal change does not justify the additional computational time, it is concluded that the result is independent of the mesh and time step.

Table 5.9: Numerical Suction Mass Flow Compared to Experiment.

Inlet Steam Quality (%)	Suction Mass Flow Experiment (g/s)	Suction Mass Flow CFD (g/s)	Mass Flow Ratio Experiment	Mass Flow Pressure Ratio CFD
8%	0.428	0.214	0.63	0.461
19%	0.996	0.272	0.80	0.521
26%	1.318	0.332	0.84	0.570
39%	1.551	0.398	0.86	0.614
47%	1.652	0.389	0.87	0.609

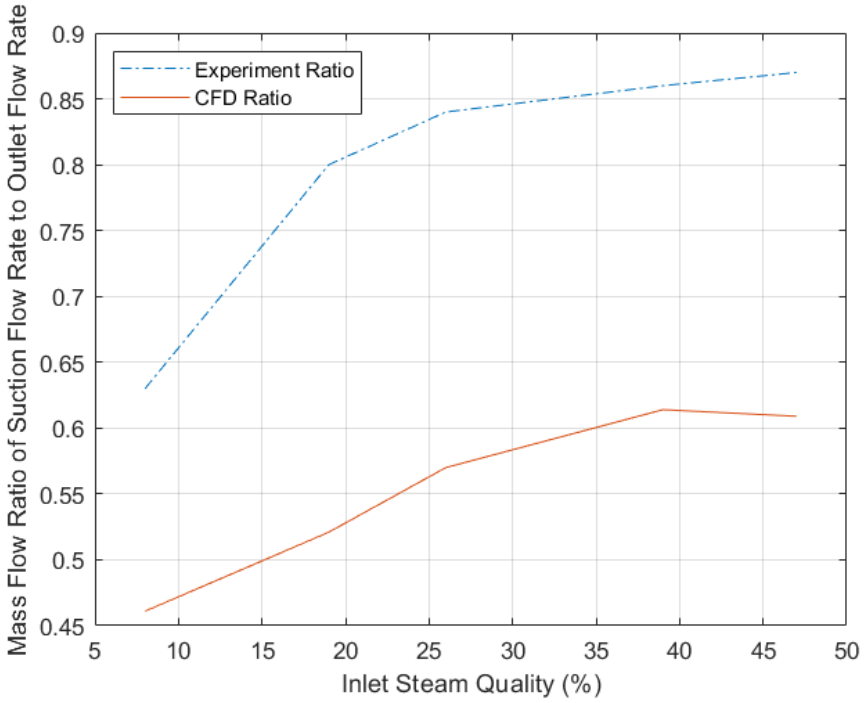

Figure 5.10: Ratio of Suction Mass Flow to Outlet Mass Flow to Inlet Steam Quality.

Table 5.10: Numerical Pressure at the Inlet and Neck Compared to Experiment.

Inlet Steam Quality (%)	Inlet Pressure Experiment (Pa)	Inlet Pressure CFD (Pa)	Neck Pressure Experiment (Pa)	Neck Pressure CFD (Pa)
8%	2250	3690	-1940	-650
19%	8250	11590	-4090	-1760
26%	14550	17180	-6320	-2730
39%	23150	25520	-8640	-4100
47%	28090	28970	-9940	-4950

Upon examining Table 5.10, it is evident that the numerical model has an increased neck pressure due to the joining flow, as also seen during the experiment. The amount by which the neck pressure increases between the two simulations is greater than between the two experiments, as seen by the higher CFD neck pressure compared to the experiment. The neck pressure is higher

due to a smaller pressure gain from neck to outlet. This may be due to an increase in friction, as there is more water in the system. However, as has been seen in calculations throughout this paper, the contribution of friction is small and not likely to be this significant. Furthermore, from the numerical results, it is seen that the pressure in the outlet region approaches zero. Therefore, the difference in pressure must come from a smaller reduction in velocity from neck to diffuser. This can only be the case if the neck velocity is lower.
The change in pressure drop from the inlet to the neck between Experiment 1 and Experiment 2 can be calculated by subtracting the values presented in Table 5.11 from those in Table 5.8. The additional resistance caused by the joining flow is expected to result in a larger pressure drop. This expectation aligns with the analytical calculation using Equation 2.25. However, the results in Table 5.12 reveal a decrease in pressure drop, rather than an increase. This difference again can only be caused by a lower velocity in the neck, leading to a smaller increase in dynamic pressure from inlet to neck and, therefore, a smaller decrease in static pressure.

Table 5.11: Pressure Drop from Inlet to Neck, of Experiment 2 and the Numerical Model.

Inlet Steam Quality (%)	Experimental Pressure Drop (Pa)	Numerical Pressure Drop (Pa)
8%	4190	4340
26%	20880	19900
47%	38030	33930

Table 5.12: Pressure Drop Increase Between the Two Experiments.

Inlet Steam Quality (%)	Pressure Drop Increase Experiment (Pa)	Pressure Drop Increase CFD (Pa)	Analytical Pressure Drop Increase (Pa)
8%	140	230	216
26%	-90	-1060	226
47%	-3540	-21360	228

Figure 5.11 illustrates the velocity of steam in the neck for both measurements with an inlet steam quality of 26%. The difference between the measurements being the joining flow in Experiment 2. It is seen that when there is a joining flow, the point of maximum velocity shifts downstream from the neck, and that the maximum steam velocity has decreased from 280 m/s to 265 m/s. A calculation of the difference in dynamic pressure due to this velocity change,

$$\Delta P = \frac{1}{2}\rho \left(u_{E1}^2 - u_{E2}^2\right) \tag{5.2}$$

gives a pressure drop reduction around 2000 Pa. When assuming that the velocity difference will be slightly lower when taking into account the water velocity and the few hundred pascals of additional pressure drop due to the joining flow, the estimation of a 1000 Pa reduction seems to be reasonable and of the correct order size given the reduction in velocity. The same calculation can be done for the higher inlet steam quality, with a velocity reduction from 460 m/s to 375 m/s, leading to a static pressure drop reduction of 21300 Pa. This confirms the hypothesis that the neck velocity is causing a decreased pressure drop from inlet to neck and a higher neck pressure. The neck velocity is being influenced by the kinetic energy transfer between the steam and the joining flow, but also condensation occurring in the neck.

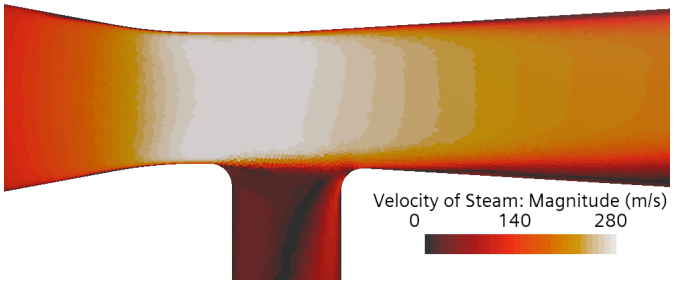

(a) Velocity of Steam in the Neck Experiment 1.

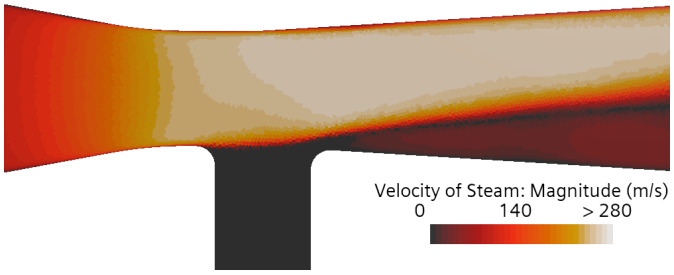

(b) Velocity of Steam in the Neck Experiment 2.

Figure 5.11: Velocity of Steam in the Neck with an Inlet Steam Quality of 26%.

The reason why the model underpredicts the neck underpressure and suction mass flow is difficult to determine. However, insights gained throughout this research may provide some possible causes. It was encountered in the single phase suction numerical model that there was a large underprediction in the suction mass flow. In that case, switching to the k-ϵ model improved the prediction of the suction mass flow. It may be the case that the turbulence of the mixing fluids is not being captured sufficiently to accurately model the suction flow. Alternatively, condensation in the outlet is known to decrease neck pressure due to the increase in velocity reduction. If the amount of condensation in the outlet is lower than that of the experiment, the underpressure in the neck and suction mass flow will be lower. This would cause the solution to converge to a value lower than that experienced in the experiment. Alternatively, the amount of condensation occurring in the neck may be over-predicted, leading to an overestimate in velocity drop in the neck.

5.4.3 Downstream Temperature

The temperature downstream from the experiment compared to the analytical results is seen in Table 5.13. The analytical results calculate a final mixture temperature using conservation of energy from Equation 2.32. For this calculation, the suction mass flow of the experiment is used. The downstream temperatures measured in the experiment are higher than the analytical temperatures calculated. This can only be the case if the fluids are not fully mixed and the measurement taken is not reading an average value. It was anticipated that the fluids would not fully mix before exiting the outlet. During the experiments, it became apparent that full condensation had not occurred, as evident by the sound the system was producing. As a result, pockets of dense water with low temperatures coexist with the hotter steam. As the temperature reading is higher than the final analytical mixture temperature, the temperature sensor is capturing mainly steam. The thermocouple was placed at the bottom of the tube to ensure water temperature is being captured. However, with the insights of CFD, it is seen that the opposite is achieved. Due to the flow direction created by the joining fluid, the condensing fluid mixture moves towards the top half of the outlet tube. This contains the majority of the water

Table 5.13: Downstream Temperature Compared to Experiment.

Inlet Steam Quality (%)	Experimental Temperature (°C)	Analytical Temperature (°C)
8%	99.3	67.6
19%	90.3	58.8
26%	89.0	57.4
39%	91.0	62.9
47%	92.0	66.5

which is being heated. The lower half of the outlet tube is mostly steam, as seen in Figure 5.12. As seen in Figure 5.13, this leads to a higher temperature reading in this region. This effect is strengthened as the tube bends downwards as seen in the experimental set up of Figure 3.4.

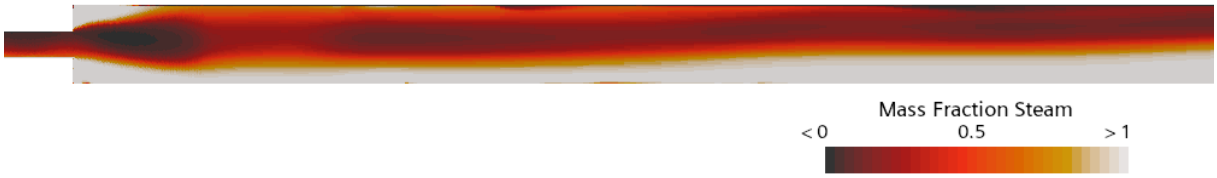

Figure 5.12: Mass Fraction Steam Distribution in the Outlet Region.

Figure 5.13: Temperature Distribution in the Outlet Region.

The downstream temperature results for the numerical model are presented in Table 5.14. These are taken at a location 3 cm from the outlet as seen in Figure 5.14. This is done to ensure that the temperature result is not influenced by reverse flow at the outlet which has a user-defined temperature. Again, the analytical mixture temperature is included. However, this calculation now uses the suction mass flow calculated in the simulation.

Table 5.14: Downstream Temperature Compared to Experiment.

Inlet Steam Quality (%)	Numerical Temperature (°C)	Analytical Temperature (°C)
8%	99.8	88.7
19%	99.1	100.0
26%	99.3	100.0
39%	101.5	100.0
47%	103.3	100.0

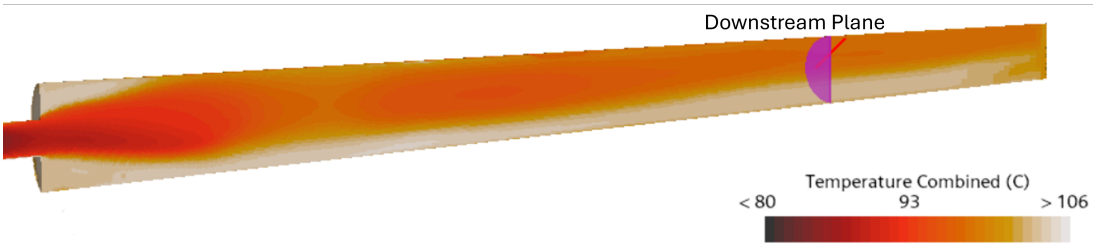

Figure 5.14: Downstream Temperature Location

As the numerical model predicts a lower suction mass flow, the temperature downstream is higher than recorded in the experiment. The underprediction of temperature relative to the analytical mixture temperature is possible. As has been encountered during this research, the heat transfer from the hot steam to the cold suction water is not instantaneous. As the fluids move through the domain, latent heat is transferred from the steam to the water. However, this does not alter the temperature of the steam, while the water heats up. This means that the mixture heats up as it moves along the domain. While the majority of heating occurs before the mixture leaves the diffuser, the last few deci-kelvin can take longer, as the temperature difference is smaller. This can be seen in the results of 19 and 26% steam quality.
Single averaged values of temperature over a plane such as in Table 5.14 should be analysed critically. Due to the multiphase nature of the numerical model, it is not possible to create a mass flow averaged result over a plane. This means that the temperature has to be surfaced averaged to get an average value over a plane. This is not a correct representation of the average for temperature. As mentioned, the mass fraction is not evenly distributed across the outlet region. The region with a higher mass flow should contribute to the solution more than a mass flow region. This leads to an error with an overprediction of temperature as seen in the higher inlet steam quality results, as the low mass regions with steam contribute as much as the higher mass regions with more water. This is a drawback of using this model, and should be known when analysing the results.

6 Conclusions and Recommendations

The objective of this research was to develop a numerical model of a venturi-driven milk foamer by utilising an Eulerian multiphase solver in Siemens Star CCM+. To achieve this goal, it was necessary to simulate saturated steam, the suction of fluid, and heat transfer between the two phases, leading to the heating of the suction fluid. While, in the case of an industrial application such as the LatteGo the suction fluid is milk, it was seen that for modelling purposes the use of water would be sufficient to understand the physical phenomena at play as milk is fundamentally not far from water. This also simplifies the model as it limits the model to two phases, and one fluid. Within the Eulerian multiphase solver, a boiling/condensation interaction between water and steam allows for the heat transfer and mass transfer between the two phases and is defined using a set of Nusselt numbers. Together with the interaction length scale, this fully defines the boiling/condensation model between the two phases.

The problem was built up by first modelling the separate physical phenomena independently. The problem was split up into two main sections; firstly, the understanding of pressure loss and modelling suction, secondly, modelling saturated steam, where boiling and condensation is encountered due to changes in pressure and when a colder suction fluid is introduced.

Semi-empirical pressure losses between the inlet and the neck were compared to CFD to get an indication of their relative contributions to pressure drop when applied to the geometry of a venturi-driven milk foamer. It is seen that the majority of the pressure drop occurs due to the change in area, leading to a change in velocity. Resistances caused by fiction and contraction are an order of magnitude smaller. It is also seen that due to the high velocity and compressible nature of the steam flowing through the venturi, the semi-empirical pressure drop is being underestimated when compared to CFD (16%). The semi-empirical pressure drop is compared to the CFD again later in the research, but also to an experiment as a benchmark, this gave the same conclusion. The ability to model suction was tested by comparing the numerical results of a one phase water venturi injector for agricultural applications from literature. The numerical model was found to simulate the ratio of suction mass flow to total outlet mass flow well over a range of pressure differences between inlet and outlet. It was revealed that the turbulence model had a significant impact on the performance of the model at predicting the suction mass flow.

A multiphase model was set up to model saturated steam using water and steam. It was necessary to create a custom inlet to create a saturated steam inlet condition. This was done using a mass flow inlet of water at a temperature below the saturation temperature at ambient pressure, and increasing the enthalpy with a volumetric heater. The power input and mass flow rate then become the two inlet conditions, as this defines the steam quality of the incoming flow. Properties such as temperature and specific enthalpy were mass averaged to be able to generate a single value per cell in the domain. Together with pressure and steam mass fraction these are the most commonly used thermodynamic properties for this application. These values were compared to those from saturated steam tables. This was done for points along the domain. It was found that the combined properties could match those of steam tables, but not throughout the domain. It was found that for this scale of device, the time it takes for heat transfer and therefore mass transfer to occur is important. The rate at which this occurred effected the model performance, such as the pressure drop in the neck. Using the last unknown of the boiling model, the interaction length scale (mean bubble size) can be tuned to match the pressure results of an experiment.

Two experiments were carried out, these were accommodated by two numerical models. The first experiment set a benchmark for pressure in the inlet and neck when only saturated

steam flows through the domain. The first numerical model could then be tuned using the unknown interaction length scale to these results. It was found that using a bubble size of 0.4 mm would allow the results of the numerical model to match those of the experiment for two of the three measurement points. For the last measurement point, the numerical pressures deviate from the experimental results. The second experiment simulated normal use of a venturi injector. Using saturated steam as a working fluid to apply suction to a reservoir of cold water. It was seen that underpressure in the neck, suction mass flow and therefore the ratio of suction mass flow to outlet mass flow are underpredicted. This is similar to what was encountered in the single phase water suction model which was compared to an experiment from literature. Therefore, it is recommended to look deeper at the effect of the turbulence model on the performance of the two fluids mixing, and the effect this has on the suction mass flow. Furthermore, the effect of using phasic turbulence, instead of mixture turbulence can be investigated. As the suction mass flow is underpredicted, the downstream temperature is also underpredicted relative to the experiment. For both sets of temperatures, a comparison is made with an analytical approximation of the mixture temperature. Despite not accurately modelling the amount of suction, the CFD can give good physical insights regardless. For example, how the placement of the downstream temperature sensor affects the results or relative differences due to input parameters. The numerical model also gives additional insights as to why the pressure in the neck rises when there is joining flow, or why the joining flow, against expectations, reduces the static pressure drop from inlet to neck. The model has the possibility to be expanded to include the suction of air in the future.

Therefore, in conclusion, the numerical model is a useful tool to be used in conjunction with other resources such as experiments. The suction mass flow cannot be accurately modelled, however, the physics has been shown to provide valuable insights.

REFERENCES

[1] A. Tramper and H. Van Maarschalkerweerd, "Nationaal Koffie - En Thee Onderzoek 2022," tech. rep., 2022.

[2] C. Andrews, "How to Make a Cappuccino," 2019. Accessed on 02-11-2024. [ONLINE]. Available: https://coffeegeek.com/guides/howtos/cappuccino-how-to/.

[3] T. Huppertz, "Foaming properties of milk: A review of the influence of composition and processing," *International Journal of Dairy Technology*, vol. 63, pp. 477–488, 11 2010.

[4] P. Walstra, *Physical chemistry of foods*. Marcel Dekker, 2003.

[5] O. Kravchuk and H. C. Deeth, "Comparison of Mechanical Agitation, Steam Injection and Air Bubbling for Foaming Milk of Different Types," *Milchwissenschaft*, vol. 64, no. 2, 2009.

[6] Koninklijke Philips N.V., "Philips LatteGo 5400-serie," 2019. Accessed on 07-11-2024. [ONLINE]. Available: https://www.philips.nl/c-e/ho/koffie/lattego/5400-series-lattego.html.

[7] Y. Çengel, M. Boles, and M. Kanoğlu, *Thermodynamics An Engineering Approach*. 9 ed., 2019.

[8] M. Holmgren, "XSteam, Thermodynamic properties of water and steam," 2012. (https://nl.mathworks.com/matlabcentral/fileexchange/9817-x-steam-thermodynamic-properties-of-water-and-steam).

[9] Siemens Digital Industries Software, "Simcenter STAR-CCM+ User Guide v. 2206.0001," 2022.

[10] Z. Zhang and Q. Chen, "Comparison of the Eulerian and Lagrangian methods for predicting particle transport in enclosed spaces," *Atmospheric Environment*, 2007.

[11] M. Saidi, M. Rismanian, M. Monjezi, M. Zendehbad, and S. Fatehiboroujeni, "Comparison between Lagrangian and Eulerian approaches in predicting motion of micron-sized particles in laminar flows," *Atmospheric Environment*, vol. 89, pp. 199–206, 6 2014.

[12] W. Ranz and W. Marshall, "Evaporation from drops–Part I and II," *Chemical Engineering Progress*, vol. 48, no. 3, p. 141, 1952.

[13] Ansys Inc, "Ansys Fluent Theory Guide," 2024.

[14] E. Hughes and Duffey R.B., "Direct contact condensation and momentum-transfer in turbulent separated flows," *International Journal of Multiphase Flow*, vol. 17, pp. 599–619, 1991.

[15] X. Huang, G. Li, and M. Wang, "CFD Simulation to the Flow Field of Venturi Injector," in *Computer and Computing Technologies in Agriculture II*, vol. 294, pp. 805–815, Springer, 2009.

[16] A. H. A M Hasan, A. Hadawey, W. Abdul-Karem, and K. F. Al-Raheem, "Theoretical and Experimental Study of Bubbly Gas-water Two Phase Flows through a Universal Venturi Tube (UVT)," *International Journal of Information Science and Education*, vol. 2, no. 1, pp. 43–58, 2012.

[17] D. Bernoulli, *Hydrodynamics*. Johann Reinhold Dulsecker, 1738.

[18] I. E. Idelchik, *Handbook of Hydraulic Resistance, 3rd Edition Revised and Augmented*. Begell House, 1996.

[19] R. W. Fox and A. T. McDonald, *Introduction to Fluid Mechanics*. CRC Press, fifth edition ed., 1 1999.

[20] R. Lockhart and R. Martinelli, "Proposed Correlation of Data for Isothermal Two-Phase, Two-Component Flow in Pipes," *Chemical Engineering Progress*, vol. 45, pp. 38–48, 1949.

[21] D. Chisholm, "A Theoretical Basis for the Lockhart-Martinelli Correlation for Two-Phase Flow," *lnternational Journal of Heat and Mass Transfer*, vol. 10, pp. 1767–1778, 1967.

[22] X. Tao and C. A. Infante Ferreira, "Heat transfer and frictional pressure drop during condensation in plate heat exchangers: Assessment of correlations and a new method," *International Journal of Heat and Mass Transfer*, vol. 135, pp. 996–1012, 2019.

[23] M. Trela, R. Kwidzinski, and M. Lackowski, "Generalization of Martinelli-Nelson method of pressure drop calculation in two-phase flows," in *E3S Web of Conferences*, 2017.

[24] S. Davoodi, R. Shahbazi, S. Esmaeili, S. Sohrabvandi, A. Mortazavian, S. Jazayeri, and A. Taslimi, "Health-Related Aspects of Milk Proteins," *Iranian Journal of Pharmaceutical Research*, vol. 15, no. 3, pp. 573–591, 2016.

[25] J. Wu, X.-l. Lu, W.-d. Wang, T.-y. Wu, X.-y. Zhang, and Y.-j. Su, "Factors Affecting Foaming Properties of Milk in Cappuccino Coffee," *Pakistan Journal of Zoology*, vol. 55, no. 1, 2022.

[26] S. Kamath, T. Huppertz, A. V. Houlihan, and H. C. Deeth, "The influence of temperature on the foaming of milk," *International Dairy Journal*, vol. 18, pp. 994–1002, 10 2008.

[27] S. Silva, A. Espiga, K. Niranjan, S. Livings, J. C. Gumy, and A. Sher, "Formation and Stability of Milk Foams," in *Bubbles in Food 2: Novelty, Health and Luxury*, pp. 153–161, Elsevier, 1 2008.

[28] K. Borcherding, P. C. Lorenzen, W. Hoffmann, and K. Schrader, "Effect of foaming temperature and varying time/temperature-conditions of pre-heating on the foaming properties of skimmed milk," *International Dairy Journal*, vol. 18, pp. 349–358, 4 2008.

[29] K. Rogers, "Pasteurization," *Encyclopedia Britannica*, 2024.

[30] R. Modi, P. Komal, I. Chauhan, A. Patel, and C. Parikshit, "Dairy and Food Engineering," tech. rep., AgriMoon, 2020.

[31] J. Anderson, "Governing Equations of Fluid Dynamics," in *Computational Fluid Dynamics*, pp. 15–51, Springer, 1992.

[32] T. Poinsot and D. Veynante, *Theoretical and Numerical Combustion*. R.T. Edwards, Inc., 3 ed., 2005.

[33] E. P. Coleman, "The Flow of Fluids in a Venturi Tube," *Transactions of the American Society of Mechanical Engineers*, vol. 28, pp. 483–497, 1 1906.

[34] F. Ozkan, M. Ozturk, and A. Baylar, "Experimental investigations of air and liquid injection by venturi tubes," *Water and Environment Journal*, vol. 20, pp. 114–122, 9 2006.

[35] L. Zhang, Z. Wei, and Q. Zhang, "Structural optimization of the low-pressure venturi injector with double suction ports based on computational fluid dynamics and orthogonal test," *Desalination and Water Treatment*, vol. 214, pp. 347–354, 2021.

[36] Z. Yu, J. Tan, and S. Wang, "Enhanced discrete phase model for multiphase flow simulation of blood flow with high shear stress," *Science Progress*, vol. 104, 1 2021.

[37] Z. Hairong, Z. Weizheng, Y. Yanpeng, and Z. Ti'en, "Comparison of Turbulence Models for Multiphase-Flow Oscillating Heat Transfer Enhancement," *Numerical Heat Transfer, Part B: Fundamentals*, vol. 66, pp. 268–280, 9 2014.

A AI Statement

During the preparation of this work, I used the Llama 3 LLM to improve language and grammar. After using this tool, I thoroughly reviewed and edited the content as needed, taking full responsibility for the final outcome.

B Results Suction Validation

Here the full results of a simulated venturi injector compared to an existing experiment from literature can be seen. The discussion and plots of the ratio for a rang of outlet pressures can be seen in subsection 5.2.

Outlet Pressure (MPa)	Suction Mass Flow (L/h)		Outlet Mass Flow (L/h)		Ratio x10^{-2}		Error Ratio (%)
	Sim	Exp	Sim	Exp	Sim	Exp	
0.00	101.36	114.48	1014.95	1155.43	9.99	9.91	0.9
0.01	90.00	93.99	999.03	1077.74	9.01	8.72	3.3
0.02	78.02	87.02	982.63	1060.29	7.94	8.21	3.3
0.03	64.51	66.63	964.42	1023.53	6.69	6.51	2.8
0.04	45.14	47.36	893.75	999.14	5.05	4.74	6.5
0.05	28.75	15.78	889.63	984.12	3.23	1.6	101.9

Table B.1: Experimental and simulated data for different outlet pressures.

C Snapshot Steam in Venturi Injector

Here a snapshot of a venturi injector for milk foaming applications can be seen. In the neck the saturated steam can be seen, furthermore this can give an estimation of the order size of the dispersed water bubbles.

Figure C.1: Snapshot Steam in Venturi Injector Video

D Material List Experiments

Data collected with catManEasy.

Sensor	Product Name	Accurarcy
Inlet pressure sensor, absolute pressure (0 - 4 bar)	TRAFAG 8473.76.8417	± 0.3%
Throat pressure sensor, gauge pressure (-1 to +1 bar)	DRUCK PNP M4070	± 0.08%
Temperature sensor	Type K thermocouples	±1C or ±0.75%
Weight scale	Mettler Toledo New Classic MF MS6001 S/01	± 0.1 g
Pump	World Precision Instruments AL-4000	± 1%
Power Analyser	Janitza UMG 96-PA	±1%

E Convergence Plots

E.1 Suction of Fluid Compared to Literature Convergence

Here the suction mass flow results for both the SST and k-ϵ model are shown. This shows how the choice of turbulence model impacted the results of suction mass flow in a venturi injector. The discussion can be read in subsection 5.2.

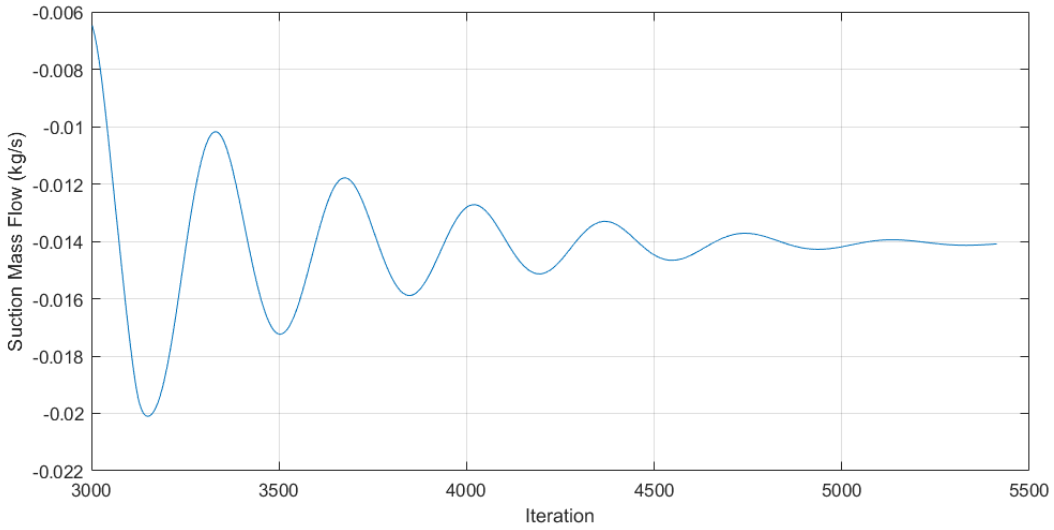

Figure E.1: Suction Mass Flow Over Time.

E.2 Final Model Convergence

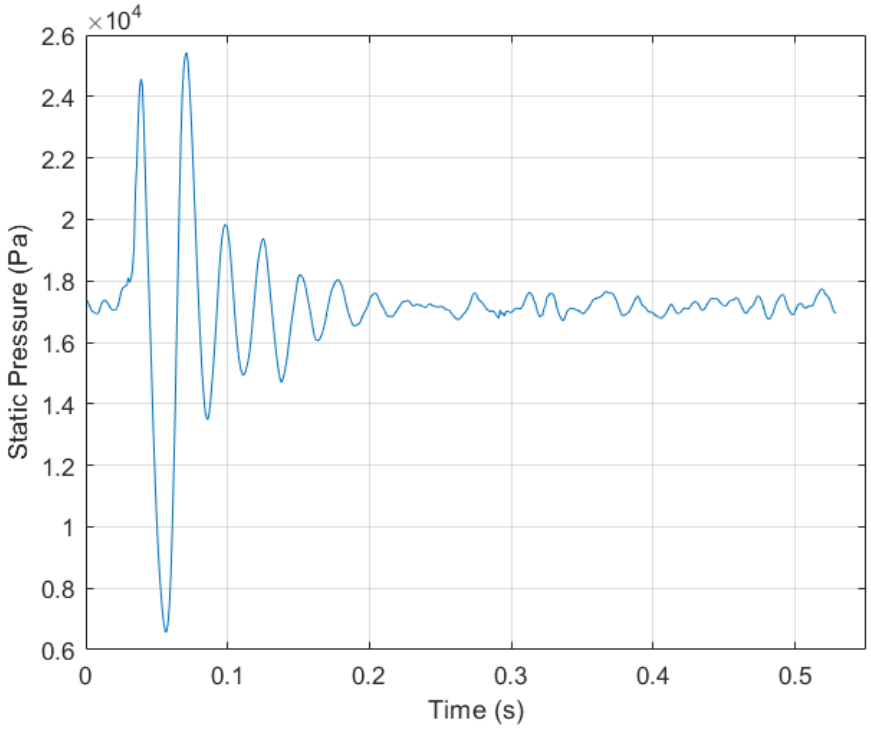

Figure E.2: Convergence of Inlet Pressure Over Time.

F Refinement

F.1 Suction of Fluid Compared to Literature Refinement

Table F.1: Suction Mass Flow of Half the Geometry for Two Mesh Densities.

Suction Mass Flow (g/s)	Number of Cells
17.32	0.5 million
17.42	2.0 million

F.2 Final Model Refinement

Table F.2: Suction Mass Flow of Half the Geometry for Two Mesh Densities.

Suction Mass Flow (g/s)	Number of Cells
0.1084	1.6 million
0.1085	2.5 million

Table F.3: Suction Mass Flow of Half the Geometry for Two Time Steps.

Suction Mass Flow (g/s)	Time Step (s)
0.1084	1e-3
0.1061	5e-4